

The role of viscosity on drop impact forces

Vatsal Sanjay^{1†}, Bin Zhang^{2‡}, Cunjing Lv^{2¶}, and Detlef Lohse^{1,3||}

¹Physics of Fluids Group, Max Planck Center for Complex Fluid Dynamics, Department of Science and Technology, and J. M. Burgers Centre for Fluid Dynamics, University of Twente, P. O. Box 217, 7500 AE Enschede, The Netherlands

²Department of Engineering Mechanics, AML, Tsinghua University, Beijing 100084, China

³Max Planck Institute for Dynamics and Self-Organization, Am Fassberg 17, 37077 Göttingen, Germany

(Received xx; revised xx; accepted xx)

A liquid drop impacting a rigid substrate undergoes deformation and spreading due to normal reaction forces, which are counteracted by surface tension. On a non-wetting substrate, the drop subsequently retracts and takes off. Our recent work (Zhang et al., *Phys. Rev. Lett.*, vol. 129, 2022, 104501) revealed two peaks in the temporal evolution of the normal force $F(t)$ – one at impact and another at jump-off. The second peak coincides with a Worthington jet formation, which vanishes at high viscosities due to increased viscous dissipation affecting flow focusing. In this article, using experiments, direct numerical simulations, and scaling arguments, we characterize both the peak amplitude F_1 at impact and the one at take off (F_2) and elucidate their dependency on the control parameters: the Weber number We (dimensionless impact kinetic energy) and the Ohnesorge number Oh (dimensionless viscosity). The first peak amplitude F_1 and the time t_1 to reach it depend on inertial timescales for low viscosity liquids, remaining nearly constant for viscosities up to 100 times that of water. For high viscosity liquids, we balance the rate of change in kinetic energy with viscous dissipation to obtain new scaling laws: $F_1/F_\rho \sim \sqrt{Oh}$ and $t_1/\tau_\rho \sim 1/\sqrt{Oh}$, where F_ρ and τ_ρ are the inertial force and time scales, respectively, which are consistent with our data. The time t_2 at which the amplitude F_2 appears is set by the inertio-capillary timescale τ_γ , independent of both the viscosity and the impact velocity of the drop. However, these properties dictate the magnitude of this amplitude.

Key words:

1. Introduction

Drop impacts have piqued the interest of scientists and artists alike for centuries, with the phenomenon being sketched by da Vinci (1508) in the early 16th and photographed by Worthington (1876a,b) in the late 19th century. It is, indeed, captivating to observe raindrops hitting a solid surface (Kim et al. 2020; Lohse & Villermaux 2020) or ocean spray affecting maritime structures (Berny et al. 2021; Villermaux et al. 2022). The phenomenology of drop impact is extremely rich, encompassing behaviors such as drop

† Email address for correspondence: vatsalsanjay@gmail.com

‡ Email address for correspondence: binzhang0710@gmail.com

¶ Email address for correspondence: cunjinglv@mail.tsinghua.edu.cn

|| Email address for correspondence: d.lohse@utwente.nl

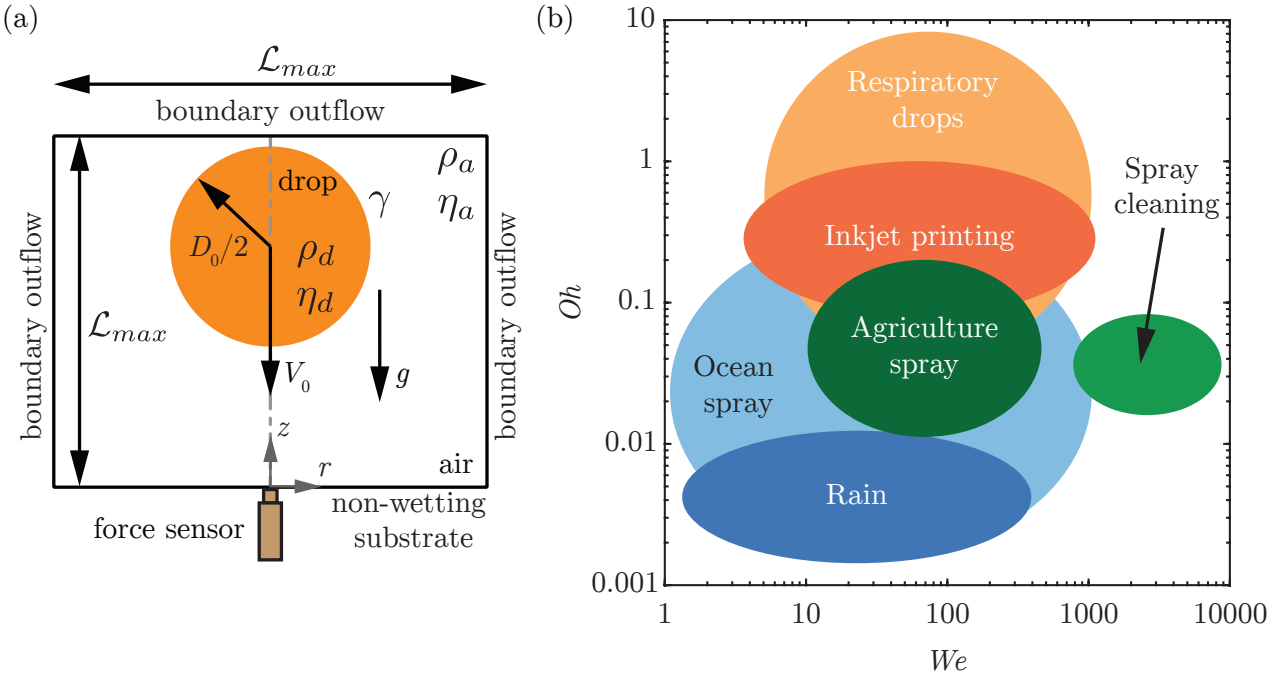


FIGURE 1. (a) Problem schematic with an axisymmetric computational domain used to study the impact of a drop with diameter D_0 and velocity V_0 on a non-wetting substrate. In the experiments, we use a quartz force sensor to measure the temporal variation of the impact force. The subscripts d and a denote the drop and air, respectively, to distinguish their material properties, which are the density ρ and the dynamic viscosity η . The drop-air surface tension coefficient is γ . The grey dashed-dotted line represents the axis of symmetry, $r = 0$. Boundary air outflow is applied at the top and side boundaries (tangential stresses, normal velocity gradient, and ambient pressure are set to zero). The domain boundaries are far enough from the drop not to influence its impact process ($\mathcal{L}_{\max} \gg D_0$, $\mathcal{L}_{\max} = 8R$ in the worst case). (b) The phase space with control parameters: the Weber number (We : dimensionless kinetic energy) and the Ohnesorge number (Oh : dimensionless viscosity), exemplifying different applications.

deformation (Biance *et al.* 2006; Moláček & Bush 2012; Chevy *et al.* 2012), spreading (Laan *et al.* 2014; Wildeman *et al.* 2016), splashing (Xu *et al.* 2005; Riboux & Gordillo 2014; Thoraval *et al.* 2021), fragmentation (Villermaux & Bossa 2011; Villermaux 2020), bouncing (Richard & Quéré 2000; Kolinski *et al.* 2014; Jha *et al.* 2020; Chubynsky *et al.* 2020; Sharma & Dixit 2021; Sanjay *et al.* 2023a), and wetting (de Gennes 1985; Fukai *et al.* 1995; Quéré 2008; Bonn *et al.* 2009). These behaviors are influenced by the interplay of inertial, capillary, and viscous forces, as well as additional factors like non-Newtonian properties (Bartolo *et al.* 2005, 2007; Smith & Bertola 2010; Gorin *et al.* 2022) of the liquid and even ambient air pressure (Xu *et al.* 2005), making the parameter space for this phenomenon both extensive and high-dimensional.

Naturally, even the process of a Newtonian liquid drop impacting a rigid substrate is governed by a plethora of control parameters, including but not limited to the drop's density ρ_d , diameter D_0 , velocity V_0 , dynamic viscosity η_d , surface tension γ , and acceleration due to gravity g (figure 1a). To navigate this rich landscape, we focus on two main dimensionless numbers that serve as control parameters (figure 1b): the Weber number We , which is the ratio of inertial to capillary forces and is given by

$$We = \frac{\rho_d V_0^2 D_0}{\gamma}, \quad (1.1)$$

and the Ohnesorge number Oh , which captures the interplay between viscous damping

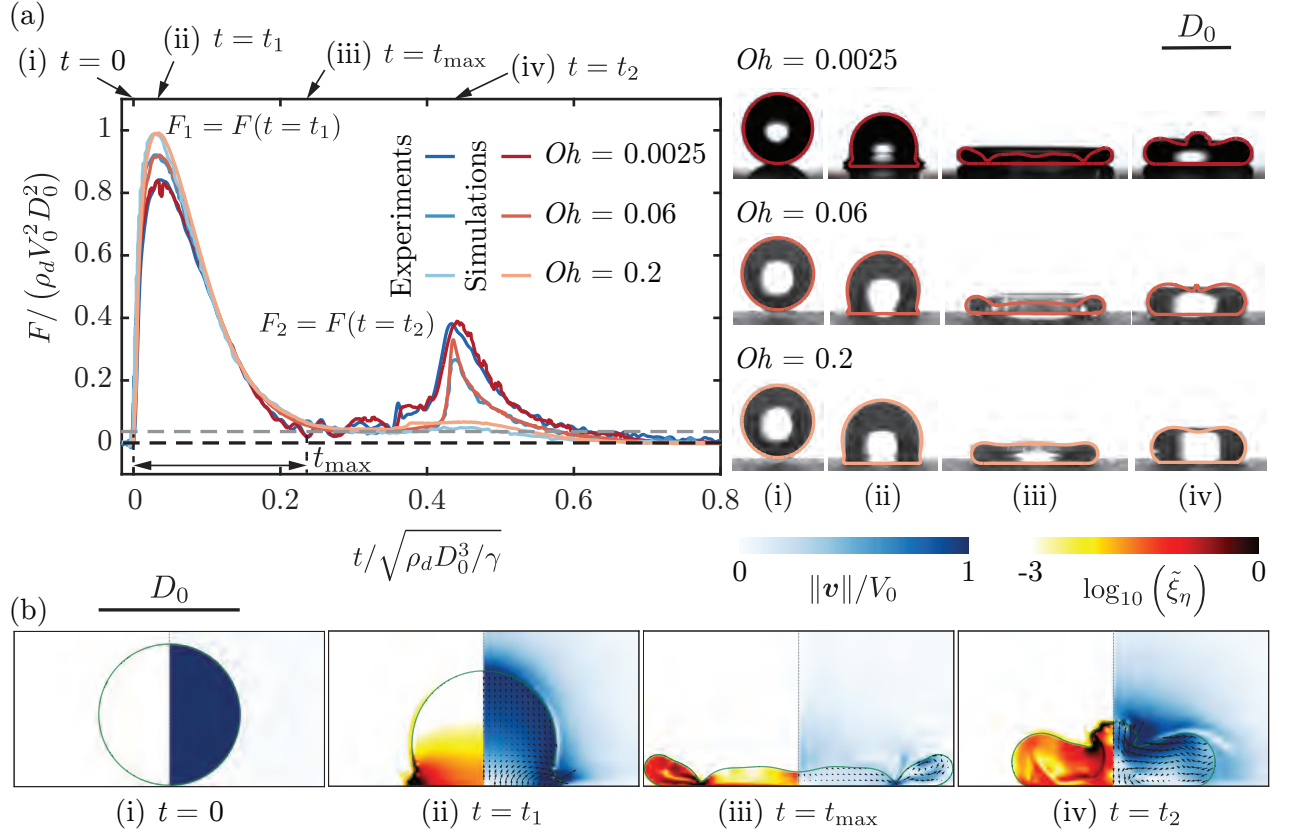


FIGURE 2. Comparison of the drop impact force $F(t)$ obtained from experiments and simulations for the three typical cases with impact velocity $V_0 = 1.2 \text{ m/s}$, 0.97 m/s , 0.96 m/s , diameter $D_0 = 2.05 \text{ mm}$, 2.52 mm , 2.54 mm , surface tension $\gamma = 72 \text{ mN/m}$, 61 mN/m , 61 mN/m and viscosity $\eta_d = 1 \text{ mPa s}$, 25.3 mPa s , 80.2 mPa s . These parameter give $Oh = 0.0025$, 0.06 , 0.2 and $We = 40$. For the three cases, the two peak amplitudes, $F_1 / (\rho_d V_0^2 D_0^2) \approx 0.82$, 0.92 , 0.99 at $t_1 \approx 0.03\sqrt{\rho_d D_0^3 / \gamma}$ and $F_2 / (\rho_d V_0^2 D_0^2) \approx 0.37$, 0.337 , 0.1 at $t_2 \approx 0.42\sqrt{\rho_d D_0^3 / \gamma}$, characterize the inertial shock from impact and the Worthington jet before takeoff, respectively. The drop reaches the maximum spreading at t_{\max} when it momentarily stops and retracts until $0.8\sqrt{\rho_d D_0^3 / \gamma}$ when the drop takes off ($F = 0$). The black and gray dashed lines in panel (a) mark $F = 0$ and the resolution $F = 0.5 \text{ mN}$ of our piezoelectric force transducer, respectively. (b) Four instances are further elaborated through numerical simulations for ($We = 40$, $Oh = 0.0025$), namely (i) $t = 0$ (touch-down), (ii) $t = 0.03\sqrt{\rho_d D_0^3 / \gamma}$ (t_1), (iii) $t = 0.2\sqrt{\rho_d D_0^3 / \gamma}$ (t_{\max}), and (iv) $t = 0.42\sqrt{\rho_d D_0^3 / \gamma}$ (t_2). The insets of panel (a) exemplify these four instances for the three representative cases illustrated here. The experimental snapshots are overlaid with the drop boundaries from simulations. We stress the excellent agreement between experiments and simulations without any free parameters. The left part of each numerical snapshot shows the dimensionless local viscous dissipation function $\tilde{\xi}_\eta \equiv \xi_\eta D_0 / (\rho_d V_0^3) = 2Oh (\tilde{\mathcal{D}} : \tilde{\mathcal{D}})$, where $\tilde{\mathcal{D}}$ is the symmetric part of the velocity gradient tensor (on a \log_{10} scale) and the right part the velocity field magnitude normalized with the impact velocity. The black velocity vectors are plotted in the center of mass reference frame of the drop to clearly elucidate the internal flow. Also see supplementary videos SM1-SM3.

and capillary oscillations, offering insights into how viscosity affects the drop's behavior upon impact,

$$Oh = \frac{\eta_d}{\sqrt{\rho_d \gamma D_0}}. \quad (1.2)$$

Additionally, the Bond number

$$Bo = \frac{\rho_d g D_0^2}{\gamma} \quad (1.3)$$

57 compares gravity to inertial forces and is needed to uniquely define the non-dimensional
58 problem.

59 The drop impact is not only interesting from the point of view of fundamental research
60 but also finds relevance in inkjet printing (Lohse 2022), the spread of respiratory drops
61 carrying airborne microbes (Bourouiba 2021; Ji *et al.* 2021; Pöhlker *et al.* 2023), cooling
62 applications (Kim 2007; Shiri & Bird 2017; Jowkar & Morad 2019), agriculture (Bergeron
63 *et al.* 2000; Bartolo *et al.* 2007; Kooij *et al.* 2018; Sijs & Bonn 2020; He *et al.* 2021;
64 Hoffman *et al.* 2021), criminal forensics (Smith *et al.* 2018; Smith & Brutin 2018), and
65 many other industrial and natural processes (Rein 1993; Yarin 2006; Tuteja *et al.* 2007;
66 Cho *et al.* 2016; Josserand & Thoroddsen 2016; Yarin *et al.* 2017; Liu *et al.* 2017; Hao
67 *et al.* 2016; Yarin *et al.* 2017; Wu *et al.* 2020). For these applications, it is pertinent to
68 understand the forces involved in drop impacts, as these forces can lead to soil erosion
69 (Nearing *et al.* 1986) or damage to engineered surfaces (Ahmad *et al.* 2013; Amirzadeh
70 *et al.* 2017; Gohardani 2011). We refer the readers to Cheng *et al.* (2022) for an overview
71 of the recent studies unraveling drop impact forces; see also Li *et al.* (2014); Soto *et al.*
72 (2014); Philippi *et al.* (2016); Zhang *et al.* (2017); Gordillo *et al.* (2018); Mitchell *et al.*
73 (2019); Zhang *et al.* (2019).

74 These forces have been studied by Zhang *et al.* (2022), employing experiments and
75 simulations and deriving scaling laws. A liquid drop impacting a non-wetting substrate
76 undergoes a series of phases—spreading, recoiling, and potentially rebounding (Chantelot
77 2018)—driven by the normal reaction force exerted by the substrate (figure 2). The
78 moment of touch-down (see figures 2a,b $t = 0$ to t_1) (Wagner 1932; Philippi *et al.* 2016;
79 Gordillo *et al.* 2018) is not surprisingly associated with a pronounced peak in the temporal
80 evolution of the drop impact force $F(t)$ owing to the sudden deceleration as high as 100
81 times the acceleration due to gravity (Clanet *et al.* 2004) (figure 2a, $F_1/(\rho_d V_0^2 D_0^2) \approx 0.82$,
82 0.92, 0.99 for $Oh = 0.0025, 0.06$, and 0.2 , respectively; at $t_1 \approx 0.03\sqrt{\rho_d D_0^3/\gamma}$). The force
83 diminishes as the drop reaches its maximum spreading diameter (figure 2a,b $t = t_m$).
84 Zhang *et al.* (2022) revealed that also the jump-off is accompanied by a peak in the normal
85 reaction force, which was up to then unknown (figure 2a, $F_2/(\rho_d V_0^2 D_0^2) \approx 0.37, 0.337$,
86 0.1 for $Oh = 0.0025, 0.06$, and 0.2 , respectively; for the second force peak amplitude—at
87 time $t_2 \approx 0.42\sqrt{\rho_d D_0^3/\gamma}$ after impact). The second peak in the force also coincides with
88 the formation of a Worthington jet, a narrow upward jet of liquid that can form due
89 to flow focusing by the retracting drop (figure 2a,b $t = t_2$). Under certain conditions
90 ($We \approx 9$, $Oh = 0.0025$), this peak can be even more pronounced than the first. This
91 discovery is critical for superhydrophobicity which is volatile and can fail due to external
92 disturbances such as pressure (Lafuma & Quéré 2003; Callies & Quéré 2005; Sbragaglia
93 *et al.* 2007; Li *et al.* 2017), evaporation (Tsai *et al.* 2010; Chen *et al.* 2012; Papadopoulos
94 *et al.* 2013), mechanical vibration (Bormashenko *et al.* 2007), or the impact forces of
95 prior droplets (Bartolo *et al.* 2006a).

96 In contrast to our prior study Zhang *et al.* (2022), which fixed the Ohnesorge number
97 to that of a 2 mm diameter water drop ($Oh = 0.0025$), our present investigation reported
98 in this paper explores a broader parameter space. We systematically and independently
99 vary the Weber and Ohnesorge numbers, extending the range of Oh to as high as 100.
100 This comprehensive approach enables us to develop new scaling laws and provides a
101 more unified understanding of the forces involved in drop impact problems. Our findings

| glycerol (wt %) | ρ_d (kg/m ³) | η_d (mPa.s) | γ (mN/m) |
|--------------------|----------------------------------|---------------------|--------------------|
| 0 | 1000 | 1 | 72 |
| 50 | 1124 | 5 | 61 |
| 63 | 1158 | 10 | 61 |
| 74 | 1188 | 25.3 | 61 |
| 80 | 1200 | 45.4 | 61 |
| 85 | 1220 | 80.2 | 61 |

TABLE 1. Properties of the water-glycerol mixtures used in the experiments. ρ_d and η_d are the density and viscosity of the drop, respectively and γ denotes the liquid-air surface tension coefficient. These properties are calculated using the protocol provided in Cheng (2008); Volk & Kähler (2018).

are particularly relevant for applications with varying viscosities and impact velocities (figure 1).

The structure of this paper is as follows: §2 briefly describes the experimental and numerical methods. §3 and §4 offer detailed analyses of the first and second peaks, respectively, focusing on their relationships with the Weber number (We) and the Ohnesorge number (Oh). Conclusions and perspectives for future research are presented in Section 5.

2. Methods

2.1. Experimental method

In the experimental setup, shown schematically in figure 1(a), a liquid drop impacts a superhydrophobic substrate. For water drops, such a surface is coated with silanized silica nanobeads with a diameter of 20 nm (Glaco Mirror Coat Zero; Soft99) resulting in the advancing and receding contact angles of $167 \pm 2^\circ$ and $154 \pm 2^\circ$, respectively (Gauthier *et al.* 2015; Li *et al.* 2017). On the other hand, for viscous aqueous glycerin drops, the upper surface is coated with an acetone solution of hydrophobic beads (Ultra ever Dry, Ultratech International, a typical bead size of 20 nm), resulting in the advancing and receding contact angles of $166 \pm 4^\circ$ and $159 \pm 2^\circ$, respectively (Jha *et al.* 2020).

The properties of the impacting drop are controlled using water-glycerol mixtures with viscosities η_d varying by almost two orders of magnitude, from 1 mPas to 80.2 mPas.

R2

Surface tension is either 72 mN/m (pure water) or 61 mN/m (glycerol), while density ρ_d ranges from 1000 kg/m³ to 1220 kg/m³, as detailed in table 1 (Cheng 2008; Volk & Kähler 2018; Jha *et al.* 2020). We note that using liquids such as silicone oil can provide a broader range of viscosity variation when paired with a superamphiphobic substrate (Deng *et al.* 2012). Additionally, employing drops of smaller radii facilitates the exploration of higher Ohnesorge numbers (Oh , see (1.2)). The drop diameter D_0 is controlled between 2.05 mm and 2.76 mm by pushing it through a calibrated needle (see appendix A for details). Consequently, we calculate Oh using the properties in table 1.

The Weber number (We , see (1.1)) is set using the impact velocity V_0 varying between 0.38 m/s and 2.96 m/s by changing the release height of the drops above the substrate. All experiments are conducted at ambient pressure and temperature. The impact force is directly measured using a high-precision piezoelectric force transducer (Kistler 9215A) with a resolution of 0.5 mN. During these measurements, the high-frequency vibrations induced by the measurement system and the surrounding noise are spectrally removed

(Implement all changes also in reply)
are of statistical nature (one standard deviation) and original from

135 using a low pass filter with a cut-off frequency of 5 kHz, following the procedure in Li *et al.*
 136 (2014); Zhang *et al.* (2017); Gordillo *et al.* (2018); Mitchell *et al.* (2019). The experiment
 137 also employs a high-speed camera (Photron Fastcam Nova S12) synchronized at 10,000
 138 fps with a shutter speed 1/20,000 s. Throughout the manuscript, the error bars ~~represent~~
 139 ~~repeated trials~~ ^{they} ~~are~~ are visible if they are larger than the marker size. We refer the
 140 readers to the supplementary material of Zhang *et al.* (2022) and appendix A for further
 141 details of the experimental setup and error characterization of the dimensionless control
 142 parameters, respectively.

R2

2.2. Numerical framework

143 In the direct numerical simulations (DNS) employed for this study, the continuity and
 144 the momentum equations take the form

$$\nabla \cdot \mathbf{v} = 0 \quad (2.1)$$

145 and

$$\frac{\partial \mathbf{v}}{\partial t} + \nabla \cdot (\mathbf{v} \mathbf{v}) = \frac{1}{\rho} (-\nabla p + \nabla \cdot (2\eta \mathcal{D}) + \mathbf{f}_\gamma) + \mathbf{g}, \quad (2.2)$$

146 respectively. Here, \mathbf{v} is the velocity field, t is time, p is pressure, and \mathbf{g} is acceleration
 147 due to gravity. We use the free software program *Basilisk C* that employs the well-
 148 balanced geometric volume of fluid (VoF) method (Popinet 2009, 2018). The VoF tracer
 149 Ψ delineates the interface between the drop (subscript d , $\psi = 1$) and air (subscript a ,
 150 $\psi = 0$), introducing a singular force $\mathbf{f}_\gamma \approx \gamma \kappa \nabla \Psi$ (κ denotes interfacial curvature, see
 151 Brackbill *et al.* 1992) to respect the dynamic boundary condition at the interface. This
 152 VoF tracer sets the material properties such that density ρ and viscosity η are given by
 153

$$\rho = \rho_a + (\rho_d - \rho_a) \Psi \quad (2.3)$$

154 and

$$\eta = \eta_a + (\eta_d - \eta_a) \Psi, \quad (2.4)$$

155 respectively. This VoF field is advected with the flow, following the equation

$$\frac{\partial \Psi}{\partial t} + \nabla \cdot (\mathbf{v} \Psi) = 0. \quad (2.5)$$

156 Lastly, we calculate the normal reaction force $\mathbf{F}(t)$ by integrating the pressure field p at
 157 the substrate,

$$\mathbf{F}(t) = \left(\int_{\mathcal{A}} (p - p_0) d\mathcal{A} \right) \hat{\mathbf{z}}, \quad (2.6)$$

158 where, p_0 , $d\mathcal{A}$, and $\hat{\mathbf{z}}$ are the ambient pressure, substrate area element, and the unit
 159 vector normal to the substrate, respectively.

160 We leverage the axial symmetry of the drop impact (figure 1a). This axial symmetry
 161 breaks at large We (≥ 100 for water drops and even larger Weber number for more
 162 viscous drops), owing to destabilization by the surrounding gas after splashing (Xu *et al.*

163 2005; Eggers *et al.* 2010; Driscoll & Nagel 2011; Riboux & Gordillo 2014; Josserand &
 164 Thoroddsen 2016; Zhang *et al.* 2022). To solve the governing equations (2.1)-(2.5), the
 165 velocity field \mathbf{v} and time t are normalized by the inertio-capillary scales, $V_\gamma = \sqrt{\gamma/\rho_d D_0}$
 166 and $\tau_\gamma = \sqrt{\rho_d D_0^3/\gamma}$, respectively. Furthermore, the pressure is normalized using the
 167 capillary pressure scale $p_\gamma = \gamma/D_0$. In such a conceptualization, Oh and We described in
 168 §1 uniquely determine the system. The Ohnesorge number based on air viscosity $Oh_a =$
 169 $(\eta_a/\eta_d) Oh$ and air-drop density ratio ρ_a/ρ_d are fixed at 10^{-5} and 10^{-3} , respectively
 170 to minimize the influence of the surrounding medium on the impact forces. Lastly, we R2

171 keep the Bond number Bo_a (see (1.3)) fixed at 1 throughout the manuscript. In our
 172 system, the relevance of gravity is characterized by the dimensionless Froude number
 173 $Fr = V_0^2/(gD_0) = We/Bo$ comparing inertia with gravity. Throughout this manuscript,
 174 $Fr > 1$ and gravity's role is sub-dominant compared to inertia (for detailed discussion,
 175 see appendix B). The substrate is modeled as a no-slip and non-penetrable wall, whereas
 176 vanishing stress and pressure are applied at the remaining boundaries to mimic outflow
 177 conditions for the surrounding air. The domain boundaries are far enough from the drop
 178 not to influence its impact process ($\mathcal{L}_{\max} \gg D_0$, $\mathcal{L}_{\max} = 8R$ in the worst case). At $t = 0$,
 179 in our simulations, we release a spherical drop whose south pole is $0.05D_0$ away from the
 180 substrate and is falling with a velocity V_0 . It is important to note that R2 experimental drops
 181 may deviate from perfect sphericity due to air drag as they fall after detaching from the
 182 needle and potential residual oscillations from detachment. These shape perturbations
 183 are more pronounced in cases with low Weber and Ohnesorge numbers. To quantify
 184 this non-sphericity, we measure the drop's aspect ratio (horizontal to vertical diameter)
 185 immediately before substrate contact. The precise pre-impact drop shape can significantly
 186 influence subsequent impact dynamics (Thoraval *et al.* 2013; Yun 2017; Zhang *et al.*
 187 2019). In our experiments, we constrain our analysis to drops with aspect ratios between
 188 0.96 and 1.05. Given this narrow range, we posit that the impact of these shape variations
 189 is negligible compared to the experimental error bars derived from repeated trials under
 190 identical nominal conditions. The simulations utilize adaptive mesh refinement to finely
 191 resolve the velocity, viscous dissipation, and the VoF tracer fields. A minimum grid size
 192 $\Delta = D_0/2048$ is used for this study.

193 To ensure a perfectly non-wetting surface, we impose a thin air layer (minimum
 194 thickness $\sim \Delta/2$) between the drop and the substrate. This air layer prevents direct
 195 contact between the liquid and solid (Kolinski *et al.* 2014; Sprittles 2024), effectively
 196 mimicking a perfectly non-wetting surface. The presence of this air layer is crucial for
 197 capturing the dynamics of drop impact on superhydrophobic surfaces, as it allows for
 198 the formation of an air cushion that can significantly affect the spreading and rebound
 199 behavior of the drop (Ramírez-Soto *et al.* 2020; Sanjay *et al.* 2023a). While this approach
 200 does not fully resolve the microscopic dynamics within the air layer itself, such as the
 201 high-velocity gradients and viscous dissipation inside the gas film once it thins below a
 202 critical size ($\sim 10\Delta$), it has been shown to accurately capture the macroscopic behavior
 203 of drop impact in the parameter range of interest (Ramírez-Soto *et al.* 2020; Sanjay
 204 *et al.* 2023b; Alventosa *et al.* 2023a; García-Geijo *et al.* 2024). We refer the readers to
 205 Sanjay (2022) for discussions about this “precursor”, air film method and to Popinet &
 206 collaborators (2013–2023); Sanjay (2024); Zhang *et al.* (2022) for details on the numerical
 207 framework.

208 3. Anatomy of the first impact force peak

209 This section elucidates the anatomy of the first impact force peak and its relationship
 210 with the Weber We and Ohnesorge Oh numbers, first for the inertial limit (§3.1, $Oh \ll 1$)

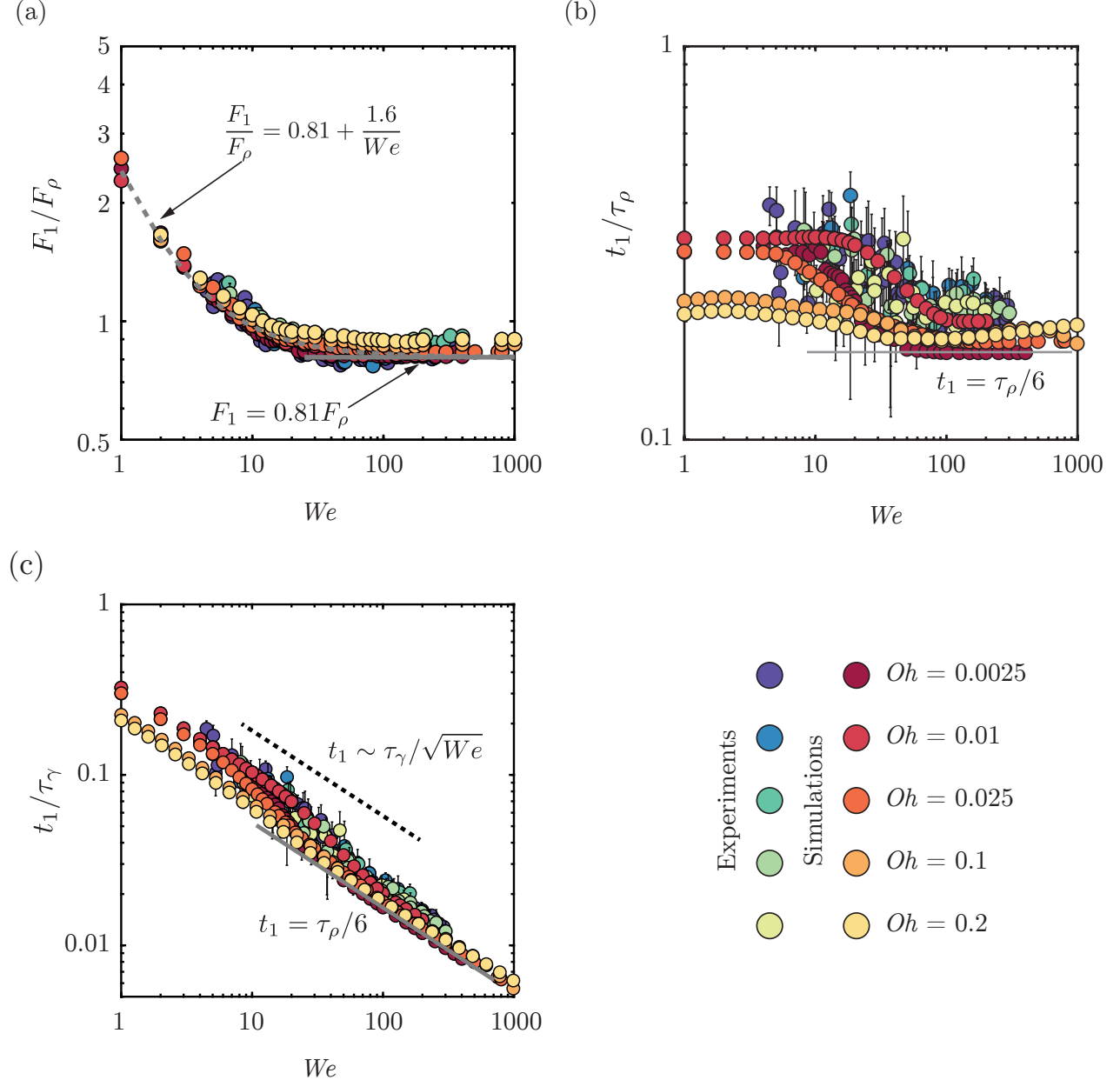


FIGURE 3. Anatomy of the first impact force peak amplitude at low Oh in between 0.0025 and 0.2, see color legend: We dependence of the (a) magnitude F_1 normalized by the inertial force scale $F_\rho = \rho_d V_0^2 D_0^2$ and time t_1 to reach the first force peak amplitude normalized by (b) the inertial timescale $\tau_\rho = D_0/V_0$ and (c) the inertia-capillary time scale $\tau_\gamma = \sqrt{\rho_d D_0^3/\gamma}$.

and then for the viscous asymptote (§3.2, $Oh \gg 1$). The results of this section are summarized in figure 3 that shows an excellent agreement between experiments and simulations without any free parameters.

3.1. Low Ohnesorge number impacts

For low Oh and large We , inertial force and time scales dictate the drop impact dynamics (figures 3 and 4). As the drop falls on a substrate, the part of the drop immediately in contact with the substrate stops moving, whereas the top of the drop still falls with the impact velocity (figure 4, from $t = t_1/4$ until $t = t_1$). Consequently, momentum conservation implies

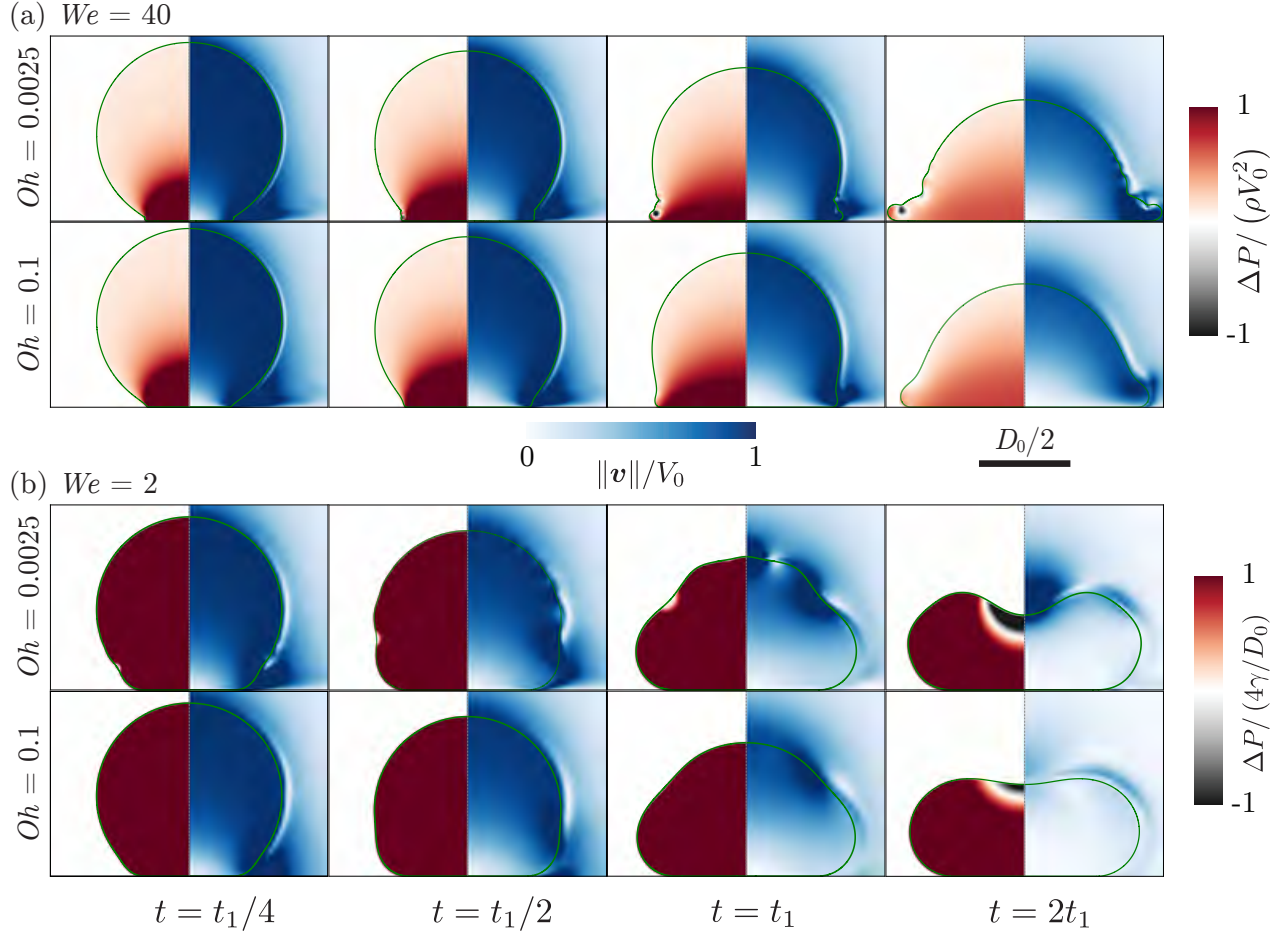


FIGURE 4. Direct numerical simulations snapshots illustrating the drop impact dynamics for $We =$ (a) 40 and (b) 2. The left-hand side of each numerical snapshot shows the pressure normalized by (a) the inertial pressure scale $\rho_d V_0^2$ and (b) the capillary pressure scale γ/D_0 . The right-hand side shows the velocity field magnitude normalized by the impact velocity V_0 .

$$F_1 \sim V_0 \frac{dm}{dt}, \quad (3.1)$$

where the mass flux $dm/dt \sim \rho_d V_0 D_0^2$ (Soto *et al.* 2014; Zhang *et al.* 2022). As a result, the first peak amplitude scales with the inertial pressure force (figure 3a)

$$F_1 \sim F_\rho, \text{ where } F_\rho = \rho_d V_0^2 D_0^2, \quad (3.2)$$

for high Weber numbers ($We > 30$, $F_1 \approx 0.81 F_\rho$). Furthermore, the time t_1 to reach F_1 follows

$$t_1 \sim \frac{D_0}{V_0} = \tau_\rho, \quad (3.3)$$

where, τ_ρ is the inertial timescale. The relation between equations (3.2) and (3.3) is apparent from the momentum conservation which implies that the impulse of the first force peak is equal to the momentum of the impacting drop, i.e., $F_1 t_1 \sim \rho_d V_0 D_0^3 = F_\rho \tau_\rho$ (see Gordillo *et al.* 2018, Zhang *et al.* 2022, and figures 3b,c). These scaling laws depend only on the inertial shock at impact and are wettability-independent (Zhang *et al.* 2017; Gordillo *et al.* 2018; Zhang *et al.* 2022). For details of the scaling law, including the

prefactors, we refer the readers to [Philippi et al. \(2016\)](#); [Gordillo et al. \(2018\)](#); [Cheng et al. \(2022\)](#).

Figure 3 further illustrates that this inertial asymptote is insensitive to viscosity variations up to 100-fold as $F_1 \sim F_\rho$ and $t_1 \sim \tau_\rho$ for $0.0025 < Oh < 0.2$. However, deviations from the inertial force and time scales are apparent for $We < 30$ (figure 3), a phenomenon also reported in earlier work ([Soto et al. 2014](#); [Zhang et al. 2022](#)). In these instances, inertia does not act as the sole governing force but instead complements surface tension, which dictates the pressure inside the drop ($p \sim \gamma/D_0$ throughout the drop for $We \lesssim 1$, figure 4b). [Zhang et al. \(2022\)](#) proposed an empirical functional dependence as

$$F_1 = \left(\alpha_1 \rho_d V_0^2 + \alpha_2 \frac{\gamma}{D_0} \right) D_0^2, \quad (3.4)$$

based on dimensional analysis, with α_1 and α_2 as free parameters which were determined to be approximately 1.6 and 0.81, respectively for water ($Oh = 0.0025$). These coefficients only deviate marginally in the current work despite the significant increase in Oh as compared to previous works ([Cheng et al. 2022](#); [Zhang et al. 2022](#)). This consistency underscores the invariance of the pressure field inside the drop to an increase in Oh (close to the impact region, figure 4a and throughout the drop, figure 4b).

3.2. Large Ohnesorge number impacts

Figure 5 reaffirms the findings of §3.1 for low Oh that the first impact peak amplitude F_1 and the time to reach this peak amplitude t_1 scale with F_ρ and τ_ρ , respectively. As the Ohnesorge number increases further, the first impact force peak amplitude normalized with F_ρ begins to increase, indicating a transition around $Oh \approx 0.1$, where viscosity starts to play a significant role. At large Oh , we observe the scaling relationship (figure 5a)

$$F_1 \sim F_\rho \sqrt{Oh}. \quad (3.5)$$

The drop's momentum is still $\rho_d V_0 D_0^3$ which must be balanced by the impulse from the substrate, $F_1 t_1$ (see §3.1, [Gordillo et al. 2018](#), [Zhang et al. 2022](#), and figure 5b). Consequently, the time t_1 follows

$$t_1 \sim \frac{\tau_\rho}{\sqrt{Oh}}. \quad (3.6)$$

Figure 5 further shows that these scaling laws are weakly dependent on the Weber number, as viscous dissipation consumes the entire initial kinetic energy of the impacting drop (figure 6). Once again, we stress that using the water-glycerol mixtures limits the range of Oh that we can probe experimentally. We further note that the first peak is robust and does not depend on the wettability of the substrate. Consequently, to compare with the existing data such as those in [Cheng et al. \(2022\)](#) with different liquids to cover a wider range of liquid viscosities and to account for the apparent We -dependence, we plot F_1 compensated with F_ρ against the impact Reynolds number $Re \equiv \sqrt{We}/Oh = V_0 D_0 / \nu_d$. For the low Re regime, such a plot allows us to describe the We dependence on the prefactor more effectively, as illustrated in figure 5(c). However, it is important to note that some scatter is still observed at high Re values, which can be attributed to the We dependence of the impact force peak amplitude. This lack of a pure scaling behavior demonstrates how the interplay between kinetic energy and viscous dissipation within the drop dictates the functional dependence of the maximum impact force on Oh .

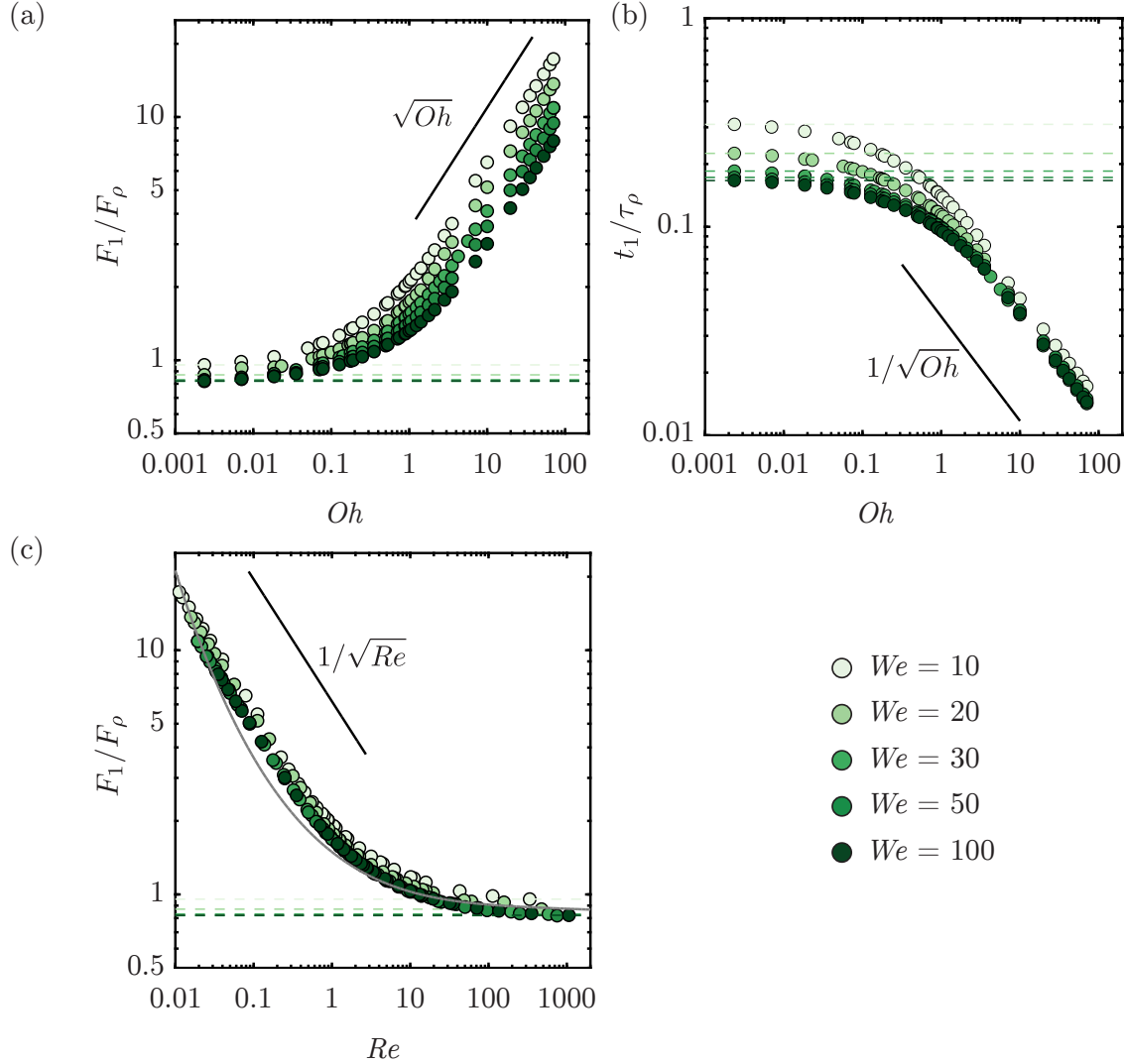


FIGURE 5. Anatomy of the first impact force peak amplitude for viscous impacts from our numerical simulations: the Oh dependence of (a) the magnitude F_1 normalized by the inertial force scale $\rho_d V_0^2 D_0^2$ and (b) the time t_1 to reach the first force peak amplitude normalized by inertial timescale $\tau_\rho = D_0/V_0$. (c) The Re dependence of the magnitude F_1 normalized by the inertial force scale $\rho_d V_0^2 D_0^2$ as compared to the (implicit) theoretical calculation of Gordillo *et al.* (2018). The black line corresponds to the scaling relationship described in §3.2. The Weber number is color-coded.

To systematically elucidate these scaling behaviors in the limit of small Re , we need to find the typical scales for the rate of change of kinetic energy and that of the rate of viscous dissipation for the drop impact system. First, we can readily define an average rate of viscous dissipation per unit mass as

$$\bar{\varepsilon} \sim \frac{1}{\tau_\rho} \frac{1}{D_0^3} \int_0^{\tau_\rho} \int_{\Omega} \nu_d (\mathcal{D} : \mathcal{D}) d\Omega dt, \quad (3.7)$$

where ν_d is the kinematic viscosity of the drop and $d\Omega$ is the volume element where dissipation occurs. Notice that $\bar{\varepsilon}$ has the dimensions of V_0^3/D_0 , i.e., length squared over time cubed or velocity squared over time, as it should be for dissipation rate of energy per unit mass. We can estimate $\Omega = D_{\text{foot}}^2 l_\nu$ (figure 6), where D_{foot} is the drop's foot diameter in contact with the substrate and l_ν is the viscous boundary layer thickness. This boundary layer marks the region of strong velocity gradients ($\sim V_0/l_\nu$) analogous to the Mirels (1955) shockwave-induced boundary layer. For details, we refer the authors to

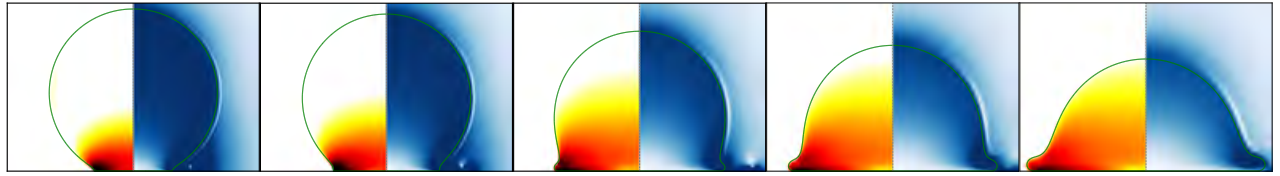
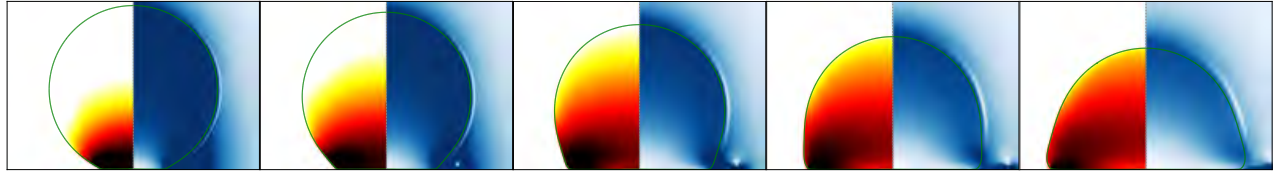
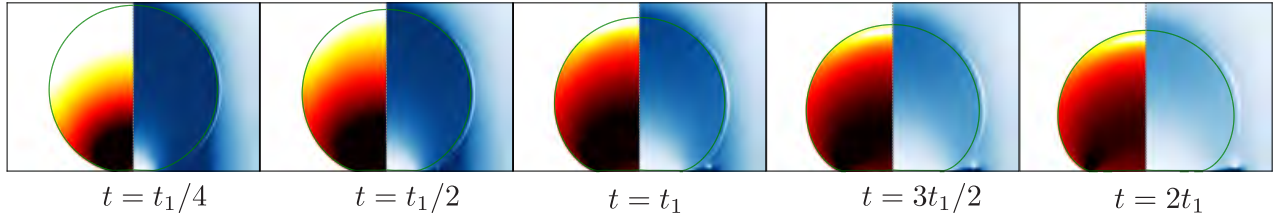
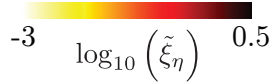
(a) $Oh = 0.05$ (b) $Oh = 0.5$ (c) $Oh = 5$  $t = t_1/4$ $t = t_1/2$ $t = t_1$ $t = 3t_1/2$ $t = 2t_1$ 

FIGURE 6. Direct numerical simulations snapshots illustrating the drop impact dynamics for $We = 100$ and $Oh =$ (a) 0.05, (b) 0.5, and (c) 5. The left-hand side of each numerical snapshot shows the viscous dissipation function ξ_η normalized by the inertial scale $\rho_d V_0^3 / D_0$. The right-hand side shows the velocity field magnitude normalized by the impact velocity V_0 .

279 Schlichting (1968); Schroll *et al.* (2010); Philippi *et al.* (2016). Consequently, the viscous
280 dissipation rate scales as

$$\bar{\varepsilon} \sim \frac{1}{\tau_\rho D_0^3} \int_0^{\tau_\rho} \nu_d \left(\frac{V_0}{l_\nu} \right)^2 D_{\text{foot}}^2 l_\nu dt. \quad (3.8)$$

281 To calculate D_{foot} , we assume that the drop maintains a spherical cap shape throughout
282 the impact (figure 6). To calculate the distance the drop would have traveled if there
283 were no substrate, we use the relation $d \sim V_0 t$. Simple geometric arguments allow us
284 to determine the relation between the foot diameter and this distance, $D_{\text{foot}} \sim \sqrt{D_0 d}$
285 (Lesser 1981; Mandre *et al.* 2009; Zheng *et al.* 2021; Bilotto *et al.* 2023; Bertin 2023).
286 Interestingly, this scaling behavior is similar to the inertial limit (Wagner 1932; Bouwhuis
287 *et al.* 2012; Philippi *et al.* 2016; Gordillo *et al.* 2019) as discussed by Langley *et al.* (2017);
288 Bilotto *et al.* (2023). Furthermore, the viscous boundary layer l_ν can be approximated
289 using $\sqrt{\nu_d t}$ (Mirels 1955; Eggers *et al.* 2010; Philippi *et al.* 2016). Filling these in (3.8),
290 we get

$$\bar{\varepsilon} \sim \frac{1}{\tau_\rho D_0^2} \int_0^{\tau_\rho} \sqrt{\nu_d} V_0^3 \sqrt{t} dt, \quad (3.9)$$

291 which on integration gives

$$\bar{\varepsilon} \sim \sqrt{\nu_d \tau_\rho} V_0^3 / D_0^2, \quad (3.10)$$

292 where τ_ρ is the inertial time scale. Here, we assume that for highly viscous drops, all

293 energy is dissipated within a fraction of τ_ρ . Filling in (3.10) and normalizing $\bar{\varepsilon}$ with the
 294 inertial scales V_0^3/D_0 ,

$$\frac{\bar{\varepsilon}}{V_0^3/D_0} \sim \sqrt{\frac{\nu_d \tau_\rho}{D_0^2}} = \frac{1}{\sqrt{Re}} = \left(\frac{Oh}{\sqrt{We}} \right)^{1/2}. \quad (3.11)$$

295 Next, the kinetic energy of the falling drop is given by

$$\dot{K}(t) \equiv \frac{dK(t)}{dt} \sim \rho_d D_0^3 \bar{\varepsilon}, \quad \text{where } K(t) = \frac{1}{2} m (V(t))^2, \quad (3.12)$$

296 and $V(t)$ is the drop's center of mass velocity. The left-hand side of (3.12) can be written
 297 as

$$\dot{K}(t) = m V(t) \frac{dV(t)}{dt} = F(t) V(t). \quad (3.13)$$

298 In equation (3.13), $F(t)$ and $V(t)$ scale with the first impact force peak amplitude F_1
 299 and the impact velocity V_0 , respectively, giving the typical scale of the rate of change of
 300 kinetic energy as

$$\dot{K}^* \sim F_1 V_0. \quad (3.14)$$

301 We stress that (3.14) states that the rate of change of kinetic energy is equal to the power
 302 of the normal reaction force, an observation already made by Wagner (1932) and Philippi
 303 *et al.* (2016) in the context of impact problems. Lastly, at large Oh , viscous dissipation
 304 enervates kinetic energy completely giving (figure 6c, also see: Philippi *et al.* (2016) and
 305 Wildeman *et al.* (2016)),

$$\dot{K}^* \sim F_1 V_0 \sim \rho_d D_0^3 \bar{\varepsilon} \quad (3.15)$$

306 Additionally, we use the inertial scales to non-dimensionalize (3.15) and fill in (3.11),
 307 giving

$$\frac{F}{F_\rho} \sim \frac{\bar{\varepsilon}}{V_0^3/D_0} \sim \frac{1}{\sqrt{Re}} = \left(\frac{Oh}{\sqrt{We}} \right)^{1/2} \quad (3.16)$$

308 and using $F_1 t_1 \sim \rho_d V_0 D_0^3 = F_\rho \tau_\rho$,

$$\frac{t_1}{\tau_\rho} \sim \left(\frac{\sqrt{We}}{Oh} \right)^{1/2}. \quad (3.17)$$

309 In summary, we use energy and momentum invariance to elucidate the parameter
 310 dependencies of the impact force as illustrated in figure 5. The scaling arguments
 311 capture the dominant force balance during the impact process, considering the relative
 312 importance of inertial, capillary, and viscous forces. As the dimensionless viscosity of
 313 impacting drops increases, the lack of surface deformation increases the normal reaction
 314 force (3.16). Further, the invariance of incoming drop momentum implies that this
 315 increase in normal reaction force occurs on a shorter timescale (3.17).

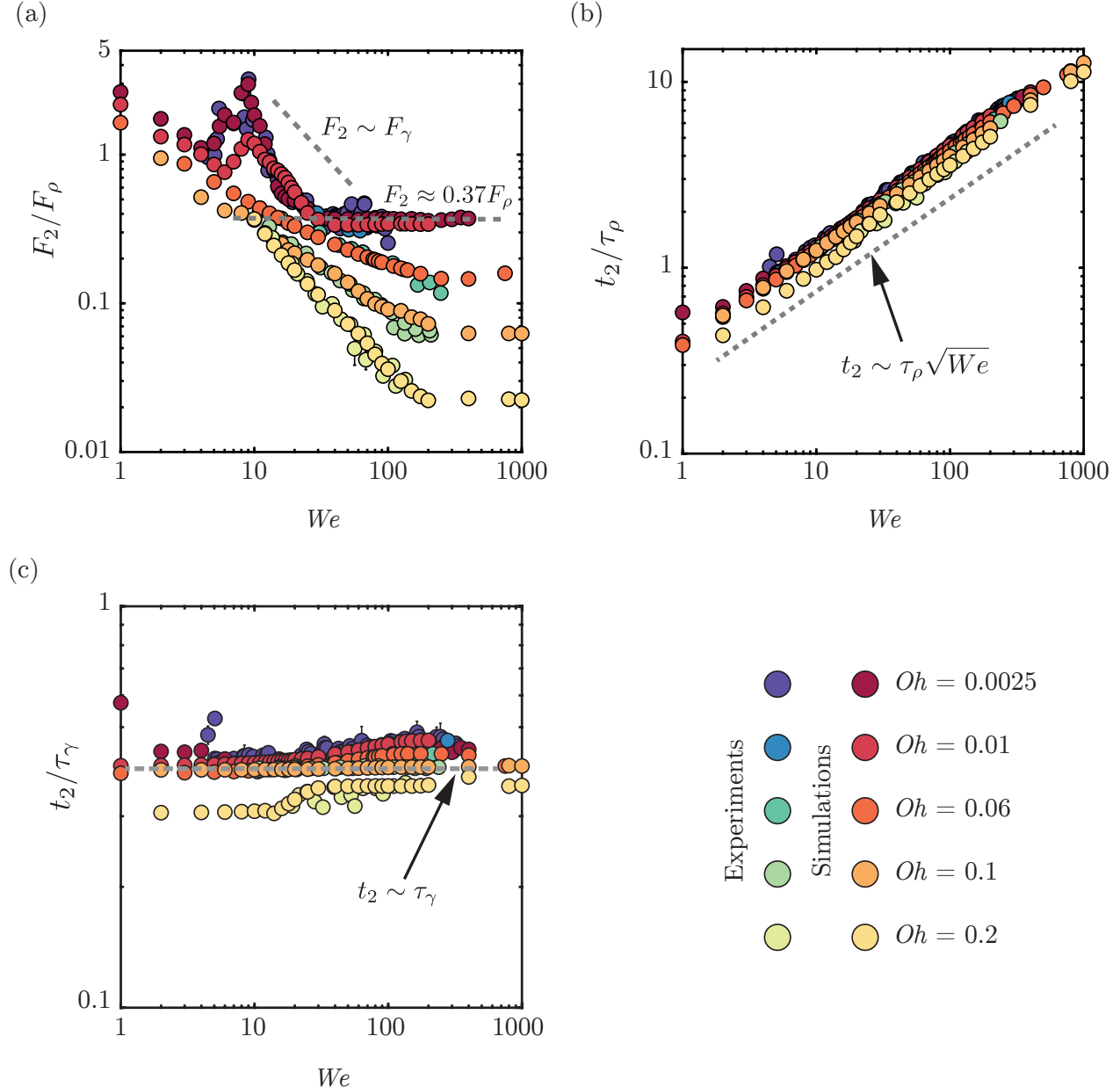


FIGURE 7. Anatomy of the second impact force peak amplitude: We dependence of the (a) magnitude F_2 normalized by the inertial force scale $F_\rho = \rho_d V_0^2 D_0^2$ and time t_2 to reach the second force peak amplitude normalized by (b) the inertio-capillary time scale $\tau_\gamma = \sqrt{\rho_d D_0^3 / \gamma}$ and (c) inertial timescale $\tau_\rho = D_0 / V_0$.

316 4. Anatomy of the second impact force peak

317 This section delves into the anatomy of the second impact force peak amplitude F_2 as a
 318 function of the Weber We and Ohnesorge Oh numbers, summarized in figure 7. We once
 319 again note the remarkable agreement between experiments and numerical simulations in
 320 this figure.

321 Similar to the mechanism leading to the formation of the first peak (§3), also the
 322 mechanism for the formation of this second peak is momentum conservation. As the
 323 drop takes off the surface, it applies a force on the substrate. As noted in §1 and Zhang
 324 *et al.* (2022), this force also coincides with the formation of a Worthington jet (figure 2iv-
 325 vi). The time t_2 at which the second peak is observed scales with the inertio-capillary
 326 timescale and is insensitive to We and Oh (figure 7b,c). Once again, we invoke the analogy
 327 between drop oscillation and drop impact to explain this behavior (Richard *et al.* 2002;

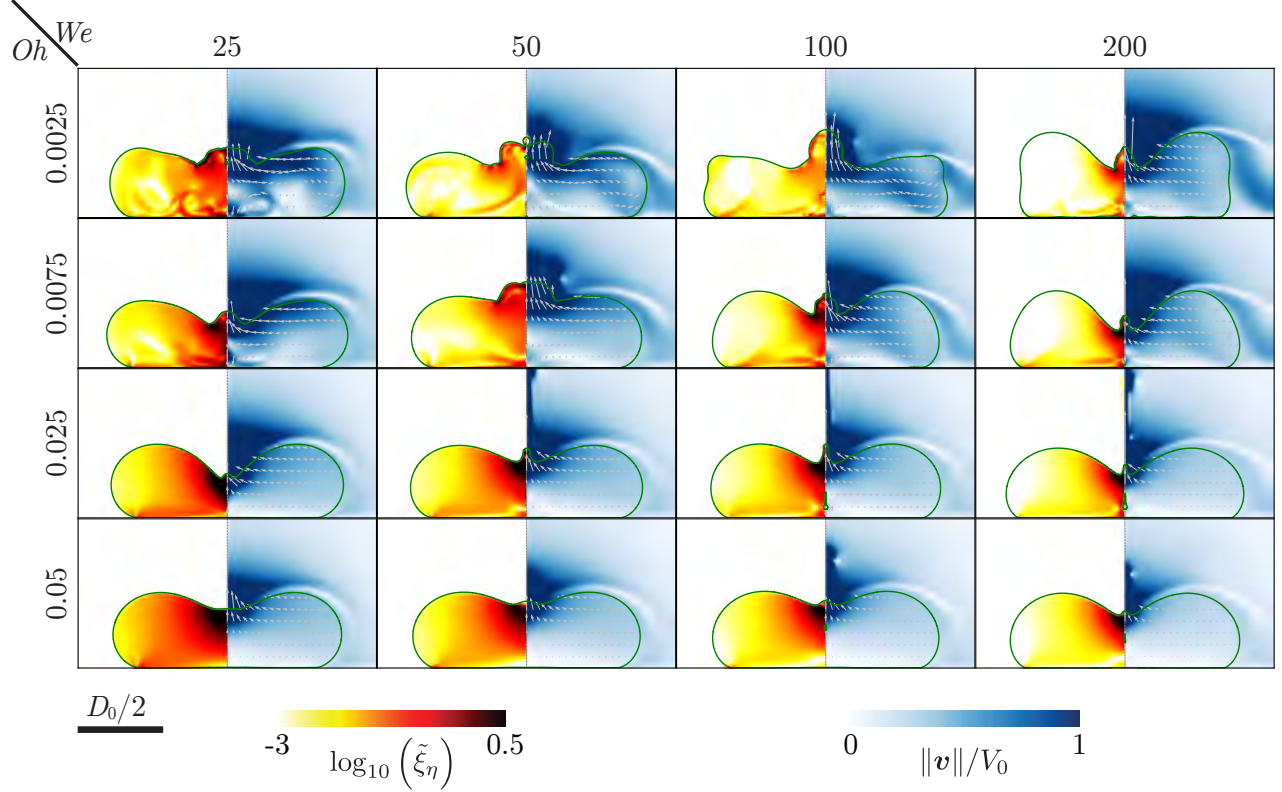


FIGURE 8. Direct numerical simulations snapshots illustrating the influence of We and Oh on the inception of the Worthington jet. All these snapshots are taken at the instant when the second peak appears in the temporal evolution of the normal reaction force ($t = t_2$). The left-hand side of each numerical snapshot shows the viscous dissipation function ξ_η normalized by the inertial scale $\rho_d V_0^3 / D_0$. The right-hand side shows the velocity field magnitude normalized by the impact velocity V_0 . The gray velocity vectors are plotted in the center of mass reference frame of the drop to clearly elucidate the internal flow.

328 Chevy et al. 2012). At the time instant $t_2 \approx 0.44\tau_\gamma$, the drop's internal motion undergoes
 329 a transition from a predominantly radial flow to a vertical one due to the formation of
 330 the Worthington jet (Chantelot 2018; Zhang et al. 2022). Figure 8 exemplifies this jet in
 331 the Oh - We parameter space, which is intricately related to the second peak in the drop
 332 impact force. For low Oh and large We , the drop retraction follows a modified Taylor-
 333 Culick dynamics (Bartolo et al. 2005; Eggers et al. 2010; Sanjay et al. 2022). As We is
 334 increased, the jet gets thinner but faster, maintaining a constant momentum flux $\rho_d V_j^2 d_j^2$,
 335 where V_j and d_j are the jet's velocity and diameter, respectively (figure 8, Zhang et al.
 336 2022). This invariance leads to the observed scaling $F_2 \sim F_\rho$ in this regime ($F_2 \approx 0.37F_\rho$
 337 for $We \geq 30, Oh \leq 0.01$).

338 Furthermore, the low We and Oh regime relies entirely on capillary pressure (figure 4).
 339 Subsequently, $F_2 \sim F_\gamma = \gamma D_0$ for $Oh < 0.01$ and $We < 30$ (figure 7). This flow focusing
 340 (figure 8) is most efficient for $We = 9$ (figure 9a, $t_2/2 < t < t_2$, Renardy et al. 2003;
 341 Bartolo et al. 2006b) where the capillary resonance leads to a thin-fast jet, accompanied
 342 by a bubble entrainment, reminiscent of the hydrodynamic singularity (figure 9, Zhang
 343 et al. 2022; Sanjay et al. 2021). The characteristic feature of this converging flow is a
 344 higher magnitude of F_2 compared to F_1 (figure 7).

345 However, this singular jet regime is very narrow in the Oh - We phase space. Figure 9b
 346 shows two cases for water drops ($Oh = 0.0025$) at different We (5 and 12 for figures 9b-
 347 i and b-ii, respectively). Bubble entrainment does not occur in either of these cases.
 348 Consequently, the maximum force amplitude diminishes for these two cases (figure 7).
 349 Nonetheless, these cases are still associated with high local viscous dissipation near the

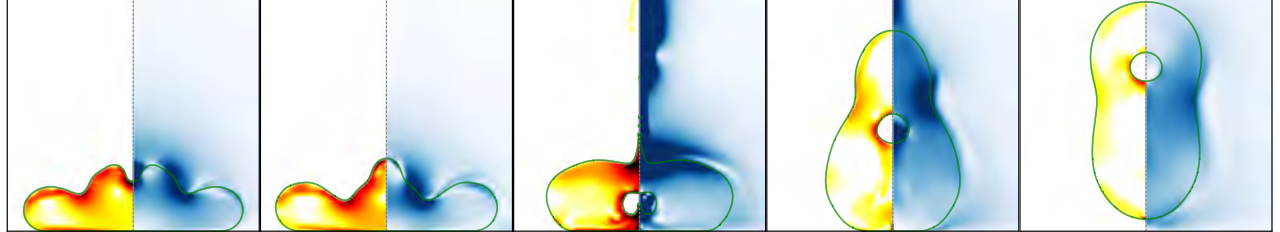
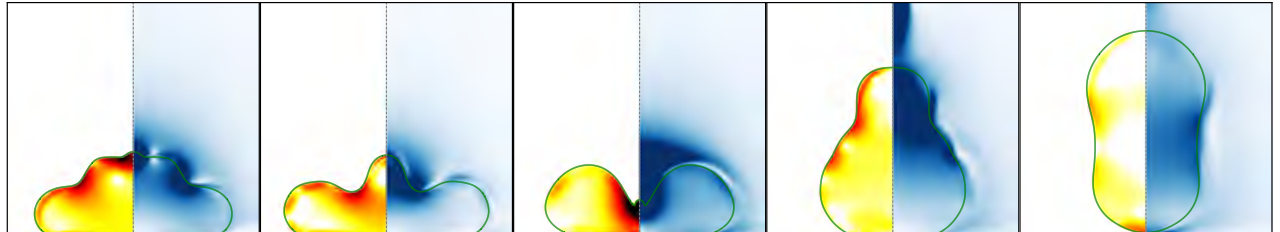
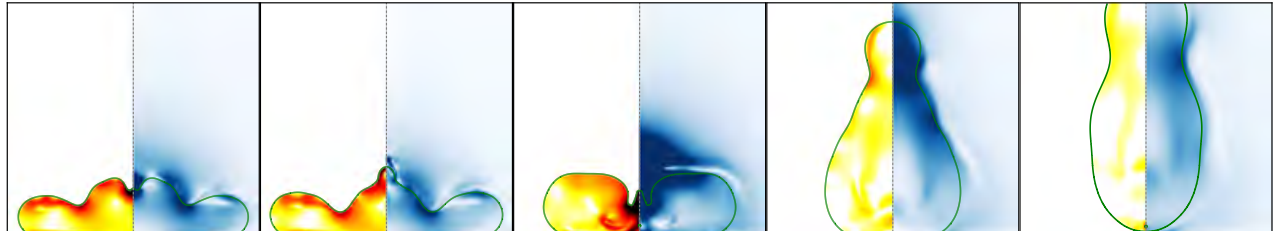
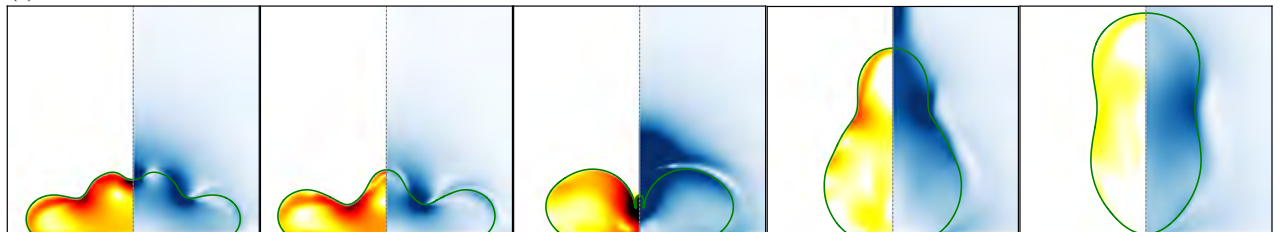
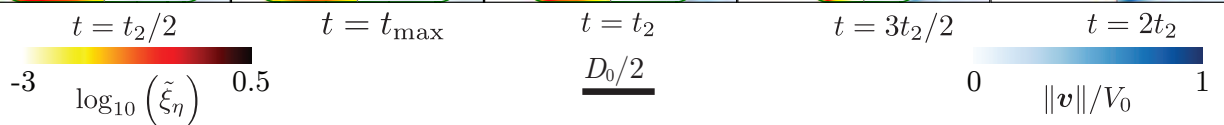
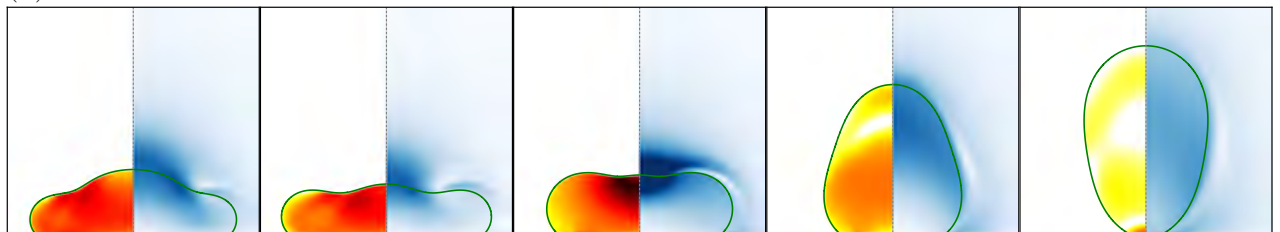
(a) $We = 9, Oh = 0.0025$ (b) $Oh = 0.0025$ (i) $We = 5$ (ii) $We = 12$ (c) $We = 9$ (i) $Oh = 0.005$ (ii) $Oh = 0.05$ 

FIGURE 9. Direct numerical simulations snapshots illustrating the influence of We and Oh on the singular Worthington jet. (a) $(We, Oh) = (9, 0.0025)$, (b) $Oh = 0.0025$ with $We =$ (i) 5 and (ii) 12, and (c) $We = 9$ with $Oh =$ (i) 0.005 and (ii) 0.05. The left-hand side of each numerical snapshot shows the viscous dissipation function ξ_η normalized by inertial scale $\rho_d V_0^3 / D_0$. The right-hand side shows the velocity field magnitude normalized by the impact velocity V_0 .

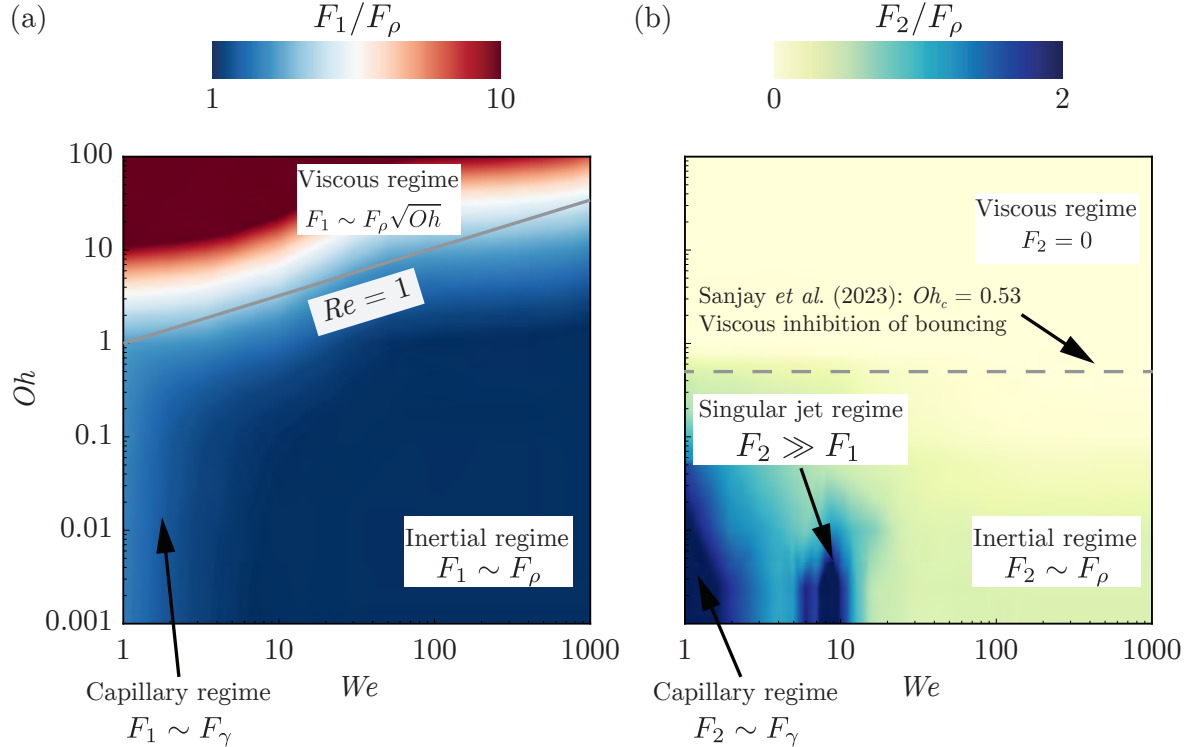


FIGURE 10. Regime map in terms of the drop Ohnesorge number Oh and the impact Weber number We to summarize the two peaks in the impact force by showing the different regimes described in this work based on (a) the first peak in the impact force peak amplitude F_1 and (b) the second peak in the impact force peak amplitude F_2 . Both peaks are normalized by the inertial force scale $F_\rho = \rho_d V_0^2 D_0^2$. These regime maps are constructed using ~ 1500 simulations in the range $0.001 \leq Oh \leq 100$ and $1 \leq We \leq 1000$. The gray solid line in (a) and dashed line in (b) mark the inertial–viscous transition ($Re = 1$) and the bouncing–no-bouncing transition ($Oh_c = 0.53$ for $Bo = 1$, see [Sanjay et al. 2023a](#)), respectively.

axis of symmetry owing to the singular nature of the flow. Another mechanism to inhibit this singular Worthington jet is viscous dissipation in the bulk. As the Ohnesorge number increases, this singular jet formation disappears ($Oh = 0.005$, figure 9c-i), significantly reducing the second peak of the impact force. For even higher viscosities, the drop no longer exhibits the sharp, focused jet formation seen at lower viscosities, and the second peak in the force is notably diminished ($Oh = 0.05$, figure 9c-ii).

Lastly, as Oh increases, bulk dissipation becomes dominant (apparent from increasing Oh at fixed We in figure 8) and can entirely inhibit drop bouncing. Recently, [Jha et al. \(2020\)](#); [Sanjay et al. \(2023a\)](#) showed that there exists a critical Oh , two orders of magnitude higher than that of a 2 mm diameter water drop, beyond which drops do not bounce either, irrespective of their impact velocity. Consequently, the second peak in the impact force diminishes for larger Oh , which explains the monotonic decrease of the amplitude F_2 observed in figure 7 for $We > 30, Oh > 0.01$.

5. Conclusion and outlook

In this work, we study the forces and dissipation encountered during the drop impact process by employing experiments, numerical simulations, and theoretical scaling laws. We vary the two dimensionless control parameters—the Weber (We : dimensionless impact kinetic energy) and the Ohnesorge number (Oh : dimensionless viscosity) independently to elucidate the intricate interplay between inertia, viscosity, and surface tension in governing the forces exerted by a liquid drop upon impact on a non-wetting substrate.

For the first impact force peak amplitude F_1 , owing to the momentum balance after

the inertial shock at impact, figure 10(a) summarizes the different regimes in the Oh - We phase space. For low Oh , inertial forces predominantly dictate the impact dynamics, such that F_1 scales with the inertial force F_ρ (Philippi *et al.* 2016; Gordillo *et al.* 2018; Mitchell *et al.* 2019; Cheng *et al.* 2022; Zhang *et al.* 2022) and is insensitive to viscosity variations up to 100-fold. As Oh increases, the viscosity becomes significant, leading to a new scaling law: $F_1 \sim F_\rho \sqrt{Oh}$. The paper unravels this viscous scaling behavior by accounting for the loss of initial kinetic energy owing to viscous dissipation inside the drop. Lastly, at low We , the capillary pressure inside the drop leads to the scaling $F_1 \sim F_\gamma$ (Moláček & Bush 2012; Chevy *et al.* 2012).

The normal reaction force described in this work is responsible for deforming the drop as it spreads onto the substrate, where it stops thanks to surface tension. If the substrate is non-wetting, it retracts to minimize the surface energy and finally takes off (Richard & Quéré 2000). In this case, the momentum conservation leads to the formation of a Worthington jet and a second peak in the normal reaction force, as summarized in figure 10(b). For low Oh and high We , the second force peak amplitude scales with the inertial force (F_ρ), following a modified Taylor-Culick dynamics (Eggers *et al.* 2010). In contrast, capillary forces dominate at low We and low Oh , leading to a force amplitude scaling of $F_2 \sim F_\gamma$. We also identify a narrow regime in the Oh - We phase space where a singular Worthington jet forms, significantly increasing F_2 (Bartolo *et al.* 2006b; Zhang *et al.* 2022), localized in the parameter space for $We \approx 9$ and $Oh < 0.01$. As Oh increases, bulk viscous dissipation counteracts this jet formation, diminishing the second peak and ultimately inhibiting drop bouncing.

Our findings have far-reaching implications, not only enriching the fundamental understanding of fluid dynamics of drop impact but also informing practical applications in diverse fields such as inkjet printing, public health, agriculture, and material science where the entire range of Oh - We phase space is relevant (figures 1b and 10). While this has identified new scaling laws, it also opens avenues for future research. For instance, it would be interesting to use the energy accounting approach to unify the scaling laws for the maximum spreading diameter for arbitrary Oh (Laan *et al.* 2014; Wildeman *et al.* 2016). Although, the implicit theoretical model summarized in Cheng *et al.* (2022) describes most of data in figure 5, we stress the importance of having a predictive model to determine F_1 for given We and Oh (Sanjay & Lohse 2024). The We influence on the impact force also warrants further exploration, especially in the regime $We \ll 1$ for arbitrary Oh (Chevy *et al.* 2012; Moláček & Bush 2012) and drop impact on compliant surfaces (Alventosa *et al.* 2023b; Ma & Huang 2023). Another potential extension of this work is to non-Newtonian fluids (Martouzet *et al.* 2021; Agüero *et al.* 2022; Bertin 2023; Jin *et al.* 2023).

Code availability. The codes used in the present article, and the parameters and data to reproduce figures 3 and 7 are permanently available at [Sanjay \(2024\)](#).

Acknowledgements. We would like to thank Vincent Bertin for comments on the manuscript. We would also like to thank Andrea Prosperetti, Pierre Chantelot, Devaraj van der Meer, and Uddalok Sen for illuminating discussions.

Funding. We acknowledge the funding by the ERC Advanced Grant No. 740479-DDD and NWO-Canon grant FIP-II. B.Z and C.L are grateful for the support from National Natural Science Foundation of China (Grant No. 12172189, 11921002, 11902179). This

JFM Notebook? Let's try!

408

409 **Code availability.** The codes used in the present article, and the parameters and data to reproduce figures 3 and 7 are permanently available at [Sanjay \(2024\)](#).

411

412 **Acknowledgements.** We would like to thank Vincent Bertin for comments on the
413 manuscript. We would also like to thank Andrea Prosperetti, Pierre Chantelot, Devaraj
414 van der Meer, and Uddalok Sen for illuminating discussions.

415

416 **Funding.** We acknowledge the funding by the ERC Advanced Grant No. 740479-DDD
417 and NWO-Canon grant FIP-II. B.Z and C.L are grateful for the support from National
418 Natural Science Foundation of China (Grant No. 12172189, 11921002, 11902179). This

R2

419 work was carried out on the national e-infrastructure of SURFsara, a subsidiary of SURF
 420 cooperation, the collaborative ICT organization for Dutch education and research. This
 421 work was sponsored by NWO - Domain Science for the use of supercomputer facilities.

422
 423 **Declaration of Interests.** The authors report no conflict of interest.

424
 425 **Author ORCID.**

426 V. Sanjay <https://orcid.org/0000-0002-4293-6099>;
 427 B. Zhang <https://orcid.org/0000-0001-8550-2584>;
 428 C. Lv <https://orcid.org/0000-0001-8016-6462>;
 429 D. Lohse <https://orcid.org/0000-0003-4138-2255>.

430

431 Appendix A. Note on the ~~parametric~~ error characterization

R2

432 This appendix outlines the methodology for characterizing experimental errors in quantification of the drop's size and impact velocities which is crucial for accurate calculation
 433 of dimensionless control parameters We and Oh . The drop diameter determination
 434 involves multiple steps. First, we measure the total mass (M_{100}) of 100 drops using an
 435 electric balance. From this mass, using the liquid density and assuming spherical shape,
 436 we calculated the drop diameter (D_0). We repeated this process five times, yielding
 437 $D_{0,1}$ through $D_{0,5}$. The average of these measurements provided the final drop diameter
 438 (D_0) and its standard error. For impact velocity determination, we extracted data from
 439 experimental high-speed imagery. By tracking the drop center's position in successive
 440 frames prior to substrate contact, and knowing the frame rate, we calculated the impact
 441 velocity. We repeated this process for five trials, obtaining $V_{0,1}$ through $V_{0,5}$. The average
 442 of these values gave the final impact velocity (V_0) and its standard error.
 443

444 The standard errors for drop diameters do not exceed 0.13 mm. For instance, drops
 445 with Ohnesorge numbers of 0.0025, 0.06, and 0.2 have diameters of 2.05 ± 0.13 mm, $2.52 \pm$
 446 0.11 mm, and 2.54 ± 0.09 mm, respectively. The standard errors for impact velocities did
 447 not exceed 0.02 m/s. For the same Oh values, the impact velocities were 1.2 ± 0.002 m/s,
 448 0.97 ± 0.01 m/s, and 0.96 ± 0.01 m/s, respectively. The combined errors in D_0 and V_0
 449 resulted in approximately $\pm 7\%$ error in Weber number We and $\pm 3\%$ error in Ohnesorge
 450 number Oh . Consequently, the horizontal error bars, which relate to errors in the control
 451 parameters, are smaller than the symbol sizes in our figures.

452 Appendix B. Role of gravity on drop impact forces

R2

453 Following table 1 and considering the variation in impacting drop diameter (appendix A), the Bond number (equation (1.3)) in our experiments ranges from 0.5 to 1.25,
 454 introducing an additional dimensionless control parameter alongside We and Oh . Gravity
 455 typically plays a negligible role in these impact processes (Sanjay *et al.* 2023a; Sanjay &
 456 Lohse 2024). We undertook a sensitivity test varying the Bond number from 0 to 1.25 in
 457 our simulations. Figure A 1 confirms the leading-order Bond invariance of the results as
 458 the impact force profiles, including both force peaks F_1 and F_2 and their corresponding
 459 times t_1 and t_2 , remain invariant to these Bond number variations. Notably, while gravity
 460 does play a role in drop impact dynamics, particularly for longer time scales and in
 461 determining the critical Ohnesorge number Oh_c for bouncing inhibition (see figure 10b
 462 and Sanjay *et al.* (2023a)), its effect on the initial impact force peaks is minimal for
 463 the parameter range studied here (large Froude numbers, $Fr > 1$). This Bond number
 464

465

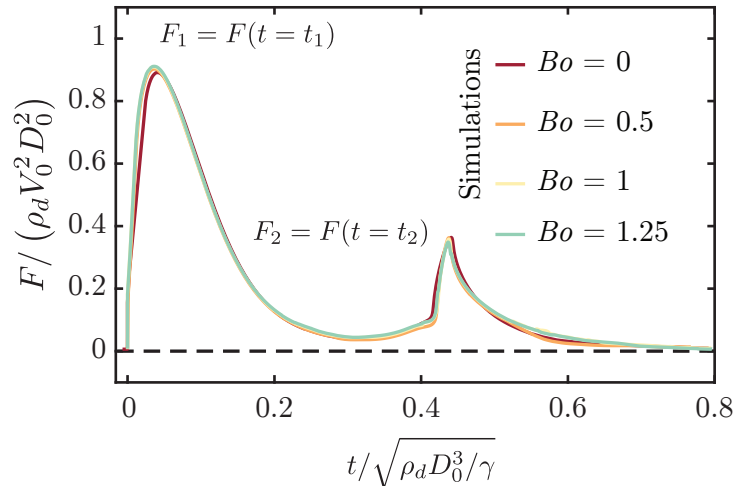


FIGURE A1. Comparison of the drop impact force $F(t)$ obtained from simulations for the four different Bond numbers $Bo = 0, 0.5, 1, 1.25$. Here, $Oh = 0.06$ and $We = 40$. Both force peaks F_1 and F_2 as well as time to reach these peaks t_1 and t_2 are invariant to variation in Bo .

invariance allows us to focus on the more dominant effects of Weber and Ohnesorge numbers. Consequently, we selected a representative value of $Bo = 1$, corresponding to a diameter of 0.00254 mm, density 1000 kg/m³, gravitational acceleration 10 m/s², and surface tension 0.061 N/m.

REFERENCES

- AGÜERO, E. A., ALVENTOSA, L. F. L., HARRIS, D. M. & GALEANO-RIOS, C. A. 2022 Impact of a rigid sphere onto an elastic membrane. *Proc. R. Soc. Lond. A* **478** (2266), 20220340.
- AHMAD, M., SCHATZ, M. & CASEY, M. V. 2013 Experimental investigation of droplet size influence on low pressure steam turbine blade erosion. *Wear* **303**, 83–86.
- ALVENTOSA, L. F. L., CIMPEANU, R. & HARRIS, D. M. 2023a Inertio-capillary rebound of a droplet impacting a fluid bath. *J. Fluid Mech.* **958**, A24.
- ALVENTOSA, L. F. L., CIMPEANU, R. & HARRIS, D. M. 2023b Inertio-capillary rebound of a droplet impacting a fluid bath. *J. Fluid Mech.* **958**, A24.
- AMIRZADEH, B., LOUGHALAM, A., RAESSI, M. & TOOTKABONI, M. 2017 A computational framework for the analysis of rain-induced erosion in wind turbine blades. *J. Wind Eng. Ind. Aerodyn.* **163**, 33–43.
- BARTOLO, D., BOUAMRIRENE, F., VERNEUIL, E., BUGUIN, A., SILBERZAN, P. & MOULINET, S. 2006a Bouncing or sticky droplets: Impalement transitions on superhydrophobic micropatterned surfaces. *Europhys. Lett.* **74** (2), 299.
- BARTOLO, D., BOUDAOU, A., NARCY, G. & BONN, D. 2007 Dynamics of non-Newtonian droplets. *Phys. Rev. Lett.* **99** (17), 174502.
- BARTOLO, D., JOSSERAND, C. & BONN, D. 2005 Retraction dynamics of aqueous drops upon impact on non-wetting surfaces. *J. Fluid Mech.* **545**, 329–338.
- BARTOLO, D., JOSSERAND, C. & BONN, D. 2006b Singular jets and bubbles in drop impact. *Phys. Rev. Lett.* **96** (12), 124501.
- BERGERON, V., BONN, D., MARTIN, J. Y. & VOVELLE, L. 2000 Controlling droplet deposition with polymer additives. *Nature* **405** (6788), 772–775.
- BERNY, A., POPINET, S., SÉON, T. & DEIKE, L. 2021 Statistics of jet drop production. *Geophys. Res. Lett.* **48** (10), e2021GL092919.
- BERTIN, V. 2023 Similarity solutions in elastohydrodynamic bouncing. *J. Fluid Mech.* **986**.
- BIANCE, A.-L., CHEVY, F., CLANET, C., LAGUBEAU, G. & QUÉRÉ, D. 2006 On the elasticity of an inertial liquid shock. *J. Fluid Mech.* **554**, 47–66.
- BILOTTO, J., KOLINSKI, J. M., LEAMPION, B., MOLINARI, J.-F., SUBHASH, G. & GARCIA-SUAREZ, J. 2023 Fluid-mediated impact of soft solids. *arXiv preprint arXiv:2311.09953*.

- 501 BONN, D., EGGERS, J., INDEKEU, J., MEUNIER, J. & ROLLEY, E. 2009 Wetting and spreading.
502 *Rev. Mod. Phys.* **81** (2), 739–805.
- 503 BORMASHENKO, E., POGREB, R., WHYMAN, G. & ERLICH, M. 2007 Resonance Cassie-Wenzel
504 wetting transition for horizontally vibrated drops deposited on a rough surface. *Langmuir*
505 **23** (24), 12217–12221.
- 506 BOUROUIBA, L. 2021 The fluid dynamics of disease transmission. *Annu. Rev. Fluid Mech.* **53**,
507 473–508.
- 508 BOUWHUIS, W., VAN DER VEEN, R. C. A., TRAN, T., KEIJ, D. L., WINKELS, K. G., PETERS,
509 I. R., VAN DER MEER, D., SUN, C., SNOEIJER, J. H. & LOHSE, D. 2012 Maximal air
510 bubble entrainment at liquid-drop impact. *Phys. Rev. Lett.* **109** (26), 264501.
- 511 BRACKBILL, J. U., KOTHE, D. B. & ZEMACH, C. 1992 A continuum method for modeling
512 surface tension. *J. Comput. Phys.* **100** (2), 335–354.
- 513 CALLIES, M. & QUÉRÉ, D. 2005 On water repellency. *Soft Matter* **1** (1), 55–61.
- 514 CHANTELOT, P. 2018 Rebonds spéciaux de liquides. PhD thesis, Université Paris-Saclay
515 (ComUE).
- 516 CHEN, X., MA, R., LI, J., HAO, C., GUO, W., LUK, B. L., LI, S. C., YAO, S. & WANG, Z.
517 2012 Evaporation of droplets on superhydrophobic surfaces: surface roughness and small
518 droplet size effects. *Phys. Rev. Lett.* **109** (11), 116101.
- 519 CHENG, N.-S. 2008 Formula for the viscosity of a glycerol–water mixture. *Ind. Eng. Chem. Res.*
520 **47** (9), 3285–3288.
- 521 CHENG, X., SUN, T.-P. & GORDILLO, L. 2022 Drop impact dynamics: impact force and stress
522 distributions. *Annu. Rev. Fluid Mech.* **54**, 57–81.
- 523 CHEVY, F., CHEPELIANSKII, A., QUÉRÉ, D. & RAPHAËL, E. 2012 Liquid Hertz contact: softness
524 of weakly deformed drops on non-wetting substrates. *Europhys. Lett.* **100** (5), 54002.
- 525 CHO, H. J., PRESTON, D. J., ZHU, Y. & WANG, E. N. 2016 Nanoengineered materials for
526 liquid–vapour phase-change heat transfer. *Nat. Rev. Mater.* **2** (2), 16092.
- 527 CHUBYNSKY, M. V., BELOUSOV, K. I., LOCKERBY, D. A. & SPRITTLES, J. E. 2020 Bouncing
528 off the walls: the influence of gas-kinetic and van der Waals effects in drop impact. *Phys.
529 Rev. Lett.* **124**, 084501.
- 530 CLANET, C., BÉGUIN, C., RICHARD, D. & QUÉRÉ, D. 2004 Maximal deformation of an
531 impacting drop. *J. Fluid Mech.* **517**, 199–208.
- 532 DA VINCI, L. 1508 *Codex Hammer* (earlier *Codex Leicester*). In *The Notebooks of Leonardo da
533 Vinci* (ed. and trans. E. MacCurdy).. George Braziller.
- 534 DE GENNES, P. G. 1985 Wetting: statics and dynamics. *Rev. Mod. Phys.* **57**, 827–863.
- 535 DENG, X., MAMMEN, L., BUTT, H.-J. & VOLLMER, D. 2012 Candle soot as a template for a
536 transparent robust superamphiphobic coating. *Science* **335** (6064), 67–70.
- 537 DRISCOLL, M. M. & NAGEL, S. R. 2011 Ultrafast interference imaging of air in splashing
538 dynamics. *Phys. Rev. Lett.* **107** (15), 154502.
- 539 EGGERS, J., FONTELOS, M. A., JOSSERAND, C. & ZALESKI, S. 2010 Drop dynamics after
540 impact on a solid wall: theory and simulations. *Phys. Fluids* **22** (6), 062101.
- 541 FUKAI, J., SHIIBA, Y., YAMAMOTO, T., MIYATAKE, O., POULIKAKOS, D., MEGARIDIS, C. M.
542 & ZHAO, Z. 1995 Wetting effects on the spreading of a liquid droplet colliding with a flat
543 surface: experiment and modeling. *Phys. Fluids* **7**, 236–247.
- 544 GARCÍA-GEIJO, P, RIBOUX, G & GORDILLO, JM 2024 The skating of drops impacting over gas
545 or vapour layers. *J. Fluid Mech.* **980**, A35.
- 546 GAUTHIER, A., SYMON, S., CLANET, C. & QUÉRÉ, D. 2015 Water impacting on
547 superhydrophobic macrotextures. *Nat. Commun.* **6** (1), 1–6.
- 548 GOHARDANI, O. 2011 Impact of erosion testing aspects on current and future flight conditions.
549 *Prog. Aerosp. Sci.* **47** (4), 280–303.
- 550 GORDILLO, J. M., RIBOUX, G. & QUINTERO, E. S. 2019 A theory on the spreading of impacting
551 droplets. *J. Fluid Mech.* **866**, 298–315.
- 552 GORDILLO, L., SUN, T.-P. & CHENG, X. 2018 Dynamics of drop impact on solid surfaces:
553 evolution of impact force and self-similar spreading. *J. Fluid Mech.* **840**, 190–214.
- 554 GORIN, B., DI MAURO, G., BONN, D. & KELLAY, H. 2022 Universal aspects of droplet spreading
555 dynamics in Newtonian and non-Newtonian fluids. *Langmuir* **38** (8), 2608–2613.
- 556 HAO, C., LIU, Y., CHEN, X., LI, J., ZHANG, M., ZHAO, Y. & WANG, Z. 2016 Bioinspired

- interfacial materials with enhanced drop mobility: from fundamentals to multifunctional applications. *Small* **12** (14), 1825–1839.
- HE, L., DING, L., LI, B., MU, W., LI, P. & LIU, F. 2021 Optimization strategy to inhibit droplets rebound on pathogen-modified hydrophobic surfaces. *ACS Appl. Mater. Interfaces* **13** (32), 38018–38028.
- HOFFMAN, H., SIJS, R., DE GOEDE, T. & BONN, D. 2021 Controlling droplet deposition with surfactants. *Phys. Rev. Fluids* **6** (3), 033601.
- JHA, A., CHANTELOT, P., CLANET, C. & QUÉRÉ, D. 2020 Viscous bouncing. *Soft Matter* **16**, 7270–7273.
- JI, B., YANG, Z. & FENG, J. 2021 Compound jetting from bubble bursting at an air-oil-water interface. *Nat. Commun.* **12** (1), 6305.
- JIN, P., ZHAO, K., BLIN, Z., ALLAIS, M., MOUTERDE, T. & QUÉRÉ, D. 2023 When marbles challenge pearls. *J. Chem. Phys.* **158** (20).
- JOSSERAND, C. & THORODDSEN, S. T. 2016 Drop impact on a solid surface. *Annu. Rev. Fluid Mech.* **48**, 365–391.
- JOWKAR, S. & MORAD, M. R. 2019 Rebounding suppression of droplet impact on hot surfaces: effect of surface temperature and concaveness. *Soft Matter* **15** (5), 1017–1026.
- KIM, J. 2007 Spray cooling heat transfer: The state of the art. *Int. J. Heat Fluid Flow* **28** (4), 753–767.
- KIM, S., WU, Z., ESMALI, E., DOMBROSKIE, J. J & JUNG, S. 2020 How a raindrop gets shattered on biological surfaces. *Proc. Natl. Acad. Sci. U.S.A.* **117** (25), 13901–13907.
- KOLINSKI, J. M., MAHADEVAN, L. & RUBINSTEIN, S. M. 2014 Drops can bounce from perfectly hydrophilic surfaces. *Europhys. Lett.* **108**, 24001.
- KOOIJ, S., SIJS, R., DENN, M. M., VILLERMAUX, E. & BONN, D. 2018 What determines the drop size in sprays? *Phys. Rev. X* **8** (3), 031019.
- LAAN, N., DE BRUIN, K. G., BARTOLO, D., JOSSERAND, C. & BONN, D. 2014 Maximum diameter of impacting liquid droplets. *Phys. Rev. Appl.* **2** (4), 044018.
- LAFUMA, A. & QUÉRÉ, D. 2003 Superhydrophobic states. *Nat. Mater.* **2** (7), 457–460.
- ANGLEY, K., LI, E. Q. & THORODDSEN, S. T. 2017 Impact of ultra-viscous drops: air-film gliding and extreme wetting. *J. Fluid Mech.* **813**, 647–666.
- LESSER, M. B. 1981 Analytic solution of liquid-drop impact problems. *Proc. R. Soc. Lond. A* **377** (1770), 289–308.
- LI, J., ZHANG, B., GUO, P. & LV, Q. 2014 Impact force of a low speed water droplet colliding on a solid surface. *J. Appl. Phys.* **116** (21), 214903.
- LI, Y., QUÉRÉ, D., LV, C. & ZHENG, Q. 2017 Monostable superrepellent materials. *Proc. Natl. Acad. Sci. USA* **114** (13), 3387–3392.
- LIU, M., WANG, S. & JIANG, L. 2017 Nature-inspired superwettability systems. *Nat. Rev. Mater.* **2** (7), 17036.
- LOHSE, D. 2022 Fundamental fluid dynamics challenges in inkjet printing. *Annu. Rev. Fluid Mech.* **54**, 349–382.
- LOHSE, D. & VILLERMAUX, E. 2020 Double threshold behavior for breakup of liquid sheets. *Proc. Natl. Acad. Sci. U.S.A.* **117**, 18912–18914.
- MA, Y. & HUANG, H. 2023 Scaling maximum spreading of droplet impacting on flexible substrates. *J. Fluid Mech.* **958**, A35.
- MANDRE, S., MANI, M. & BRENNER, M. P. 2009 Precursors to splashing of liquid droplets on a solid surface. *Phys. Rev. Lett.* **102** (13), 134502.
- MARTOUZET, G., JØRGENSEN, L., PELET, Y., BIANCE, A.-L. & BARENTIN, C. 2021 Dynamic arrest during the spreading of a yield stress fluid drop. *Phys. Rev. Fluids* **6** (4), 044006.
- MIRELS, H. 1955 Laminar boundary layer behind shock advancing into stationary fluid. *NACA TN* **3401**, 25.
- MITCHELL, B. R., KLEWICKI, J. C., KORKOLIS, Y. P. & KINSEY, B. L. 2019 The transient force profile of low-speed droplet impact: measurements and model. *J. Fluid Mech.* **867**, 300–322.
- MOLÁČEK, J. & BUSH, J. W. M. 2012 A quasi-static model of drop impact. *Phys. Fluids* **24** (12), 127103.
- NEARING, M. A., BRADFORD, J. M. & HOLTZ, R. D. 1986 Measurement of force vs. time relations for waterdrop impact. *Soil Sci. Soc. Am. J.* **50**, 1532–1536.

- 614 PAPADOPOULOS, P., MAMMEN, L., DENG, X., VOLLMER, D. & BUTT, H.-J. 2013 How
615 superhydrophobicity breaks down. *Proc. Natl Acad. Sci. USA* **110** (9), 3254–3258.
- 616 PHILIPPI, J., LAGRÉE, P.-Y. & ANTKOWIAK, A. 2016 Drop impact on a solid surface: short-time
617 self-similarity. *J. Fluid Mech.* **795**, 96–135.
- 618 PÖHLKER, M. L., PÖHLKER, C., KRÜGER, O. O., FÖRSTER, J.-D., BERKEMEIER, T., ELBERT,
619 W., FRÖHLICH-NOWOISKY, J., PÖSCHL, U., BAGHERI, G., BODENSCHATZ, E., HUFFMAN,
620 J. A., SCHEITHAUER, S. & MIKHAILOV, E. 2023 Respiratory aerosols and droplets in the
621 transmission of infectious diseases. *Rev. Mod. Phys.* **95** (4), 045001.
- 622 POPINET, S. 2009 An accurate adaptive solver for surface-tension-driven interfacial flows. *J.
623 Comput. Phys.* **228** (16), 5838–5866.
- 624 POPINET, S. 2018 Numerical models of surface tension. *Annu. Rev. Fluid Mech.* **50**, 49–75.
- 625 POPINET, S. & COLLABORATORS 2013–2023 Basilisk C: volume of fluid method. <http://basilisk.fr> (Last accessed: August 23, 2023).
- 626 QUÉRÉ, D. 2008 Wetting and roughness. *Annu. Rev. Mater. Res.* **38**, 71–99.
- 627 RAMÍREZ-SOTO, O., SANJAY, V., LOHSE, D., PHAM, J. T. & VOLLMER, D. 2020 Lifting a sessile
628 drop from a superamphiphobic surface with an impacting one. *Sci. Adv.* **6**, eaba4330.
- 629 REIN, M. 1993 Phenomena of liquid drop impact on solid and liquid surfaces. *Fluid Dyn. Res.*
630 **12**, 61–93.
- 631 RENARDY, Y., POPINET, S., DUCHEMIN, L., RENARDY, M., ZALESKI, S., JOSSERAND, C.,
632 DRUMRIGHT-CLARKE, M. A., RICHARD, D., CLANET, C. & QUÉRÉ, D. 2003 Pyramidal
633 and toroidal water drops after impact on a solid surface. *J. Fluid Mech.* **484**, 69–83.
- 634 RIBOUX, G. & GORDILLO, J. M. 2014 Experiments of drops impacting a smooth solid surface:
635 a model of the critical impact speed for drop splashing. *Phys. Rev. Lett.* **113** (2), 024507.
- 636 RICHARD, D., CLANET, C. & QUÉRÉ, D. 2002 Contact time of a bouncing drop. *Nature*
637 **417** (6891), 811–811.
- 638 RICHARD, D. & QUÉRÉ, D. 2000 Bouncing water drops. *Europhys. Lett.* **50** (6), 769–775.
- 639 SANJAY, V. 2022 Viscous Free-Surface Flows. PhD thesis, University of Twente.
- 640 SANJAY, V. 2024 Code repository: The role of viscosity on drop impact forces. <https://zenodo.org/doi/10.5281/zenodo.13381995> (Last accessed: Aug 28, 2024).
- 641 SANJAY, V., CHANTELOT, P. & LOHSE, D. 2023a When does an impacting drop stop bouncing?
642 *Journal of Fluid Mechanics* **958**, A26.
- 643 SANJAY, V., LAKSHMAN, S., CHANTELOT, P., SNOEIJER, J. H. & LOHSE, D. 2023b Drop impact
644 on viscous liquid films. *J. Fluid Mech.* **958**, A25.
- 645 SANJAY, V. & LOHSE, D. 2024 Unifying theory of scaling in drop impact: Forces & maximum
646 spreading diameter. *arXiv preprint arXiv: 2408.12714*.
- 647 SANJAY, V., LOHSE, D. & JALAAL, M. 2021 Bursting bubble in a viscoplastic medium. *J. Fluid
648 Mech.* **922**, A2.
- 649 SANJAY, V., SEN, U., KANT, P. & LOHSE, D. 2022 Taylor-Culick retractions and the influence
650 of the surroundings. *J. Fluid Mech.* **948**, A14.
- 651 SBRAGAGLIA, M., PETERS, A. M., PIRAT, C., BORKENT, B. M., LAMMERTINK, R. G. H.,
652 WESSLING, M. & LOHSE, D. 2007 Spontaneous breakdown of superhydrophobicity. *Phys.
653 Rev. Lett.* **99** (15), 156001.
- 654 SCHLICHTING, H. 1968 *Boundary-layer theory*. McGraw-Hill.
- 655 SCHROLL, R. D., JOSSERAND, C., ZALESKI, S. & ZHANG, W. W. 2010 Impact of a viscous
656 liquid drop. *Phys. Rev. Lett.* **104** (3), 034504.
- 657 SHARMA, P. K. & DIXIT, H. N. 2021 Regimes of wettability-dependent and wettability-
658 independent bouncing of a drop on a solid surface. *J. Fluid Mech.* **908**, A37.
- 659 SHIRI, S. & BIRD, J. C. 2017 Heat exchange between a bouncing drop and a superhydrophobic
660 substrate. *Proc. Natl. Acad. Sci. U.S.A.* **114** (27), 6930–6935.
- 661 SIJS, R. & BONN, D. 2020 The effect of adjuvants on spray droplet size from hydraulic nozzles.
662 *Pest. Manage. Sci.* **76** (10), 3487–3494.
- 663 SMITH, F. R. & BRUTIN, D. 2018 Wetting and spreading of human blood: recent advances and
664 applications. *Curr. Opin. Colloid Interface Sci.* **36**, 78–83.
- 665 SMITH, F. R., NICLOUX, C. & BRUTIN, D. 2018 Influence of the impact energy on the pattern
666 of blood drip stains. *Phys. Rev. Fluids* **3** (1), 013601.
- 667 SMITH, M. I. & BERTOLA, V. 2010 Effect of polymer additives on the wetting of impacting
668 droplets. *Phys. Rev. Lett.* **104**, 154502.
- 669

- 671 SOTO, D., DE LARIVIERE, A. B., BOUTILLON, X., CLANET, C. & QUÉRÉ, D. 2014 The force
672 of impacting rain. *Soft Matter* **10** (27), 4929–4934.
- 673 SPRITTLES, JAMES E 2024 Gas microfilms in droplet dynamics: When do drops bounce? *Annu.*
674 *Rev. Fluid Mech.* **56**, 91–118.
- 675 THORAVAL, M.-J., SCHUBERT, J., KARPITSCHKA, S., CHANANA, M., BOYER, F., SANDOVAL-
676 NAVAL, E., DIJKSMAN, J. F., SNOEIJER, J. H. & LOHSE, D. 2021 Nanoscopic interactions
677 of colloidal particles can suppress millimetre drop splashing. *Soft Matter* **17** (20), 5116–
678 5121.
- 679 THORAVAL, M.-J., TAKEHARA, K., ETOH, T. G. & THORODDSEN, S. T. 2013 Drop impact
680 entrapment of bubble rings. *J. Fluid Mech.* **724**, 234–258.
- 681 TSAI, P., LAMMERTINK, R. G. H., WESSLING, M. & LOHSE, D. 2010 Evaporation-triggered
682 wetting transition for water droplets upon hydrophobic microstructures. *Phys. Rev. Lett.*
683 **104** (11), 116102.
- 684 TUTEJA, A., CHOI, W., MA, M., MABRY, J. M., MAZZELLA, S. A., RUTLEDGE, G. C.,
685 MCKINLEY, G. H. & COHEN, R. E. 2007 Designing superoleophobic surfaces. *Science*
686 **318** (5856), 1618–1622.
- 687 VILLERMAUX, E. 2020 Fragmentation versus cohesion. *J. Fluid Mech.* **898**, P1.
- 688 VILLERMAUX, E. & BOSSA, B. 2011 Drop fragmentation on impact. *J. Fluid Mech.* **668**, 412–
689 435.
- 690 VILLERMAUX, E., WANG, X. & DEIKE, L. 2022 Bubbles spray aerosols: certitudes and mysteries.
691 *Proc. Natl. Acad. Sci. Nexus* **1** (5), pgac261.
- 692 VOLK, A. & KÄHLER, C. J. 2018 Density model for aqueous glycerol solutions. *Exp. Fluids*
693 **59** (5), 75.
- 694 WAGNER, H. 1932 Über Stoß- und Gleitvorgänge an der Oberfläche von Flüssigkeiten. *Z. Angew.*
695 *Math. Mech.* **12** (4), 193–215.
- 696 WILDEMAN, S., VISSER, C. W., SUN, C. & LOHSE, D. 2016 On the spreading of impacting
697 drops. *J. Fluid Mech.* **805**, 636–655.
- 698 WORTHINGTON, A. M. 1876a On the forms assumed by drops of liquids falling vertically on a
699 horizontal plate. *Proc. R. Soc.* **25** (171–178), 261–272.
- 700 WORTHINGTON, A. M. 1876b A second paper on the forms assumed by drops of liquids falling
701 vertically on a horizontal plate. *Proc. R. Soc.* **25** (171–178), 498–503.
- 702 WU, S., DU, Y., ALSAID, Y., WU, D., HUA, M., YAN, Y., YAO, B., MA, Y., ZHU, X. & HE,
703 X. 2020 Superhydrophobic photothermal icephobic surfaces based on candle soot. *Proc.*
704 *Natl Acad. Sci. USA* **117** (21), 11240–11246.
- 705 XU, L., ZHANG, W. W. & NAGEL, S. R. 2005 Drop splashing on a dry smooth surface. *Phys.*
706 *Rev. Lett.* **94** (18), 184505.
- 707 YARIN, A. L. 2006 Drop impact dynamics: splashing, spreading, receding, bouncing... *Annu.*
708 *Rev. Fluid Mech.* **38**, 159–192.
- 709 YARIN, A. L., ROISMAN, I. V. & TROPEA, C. 2017 *Collision Phenomena in Liquids and Solids*.
710 Cambridge University Press.
- 711 YUN, S. 2017 Bouncing of an ellipsoidal drop on a superhydrophobic surface. *Sci. Rep.* **7** (1),
712 17699.
- 713 ZHANG, B., LI, J., GUO, P. & LV, Q. 2017 Experimental studies on the effect of reynolds and
714 weber numbers on the impact forces of low-speed droplets colliding with a solid surface.
715 *Exp. Fluids* **58** (9), 1–12.
- 716 ZHANG, B., SANJAY, V., SHI, S., ZHAO, Y., LV, C. & LOHSE, D. 2022 Impact forces of water
717 drops falling on superhydrophobic surfaces. *Phys. Rev. Lett.* **129**, 104501.
- 718 ZHANG, R., ZHANG, B., LV, Q., LI, J. & GUO, P. 2019 Effects of droplet shape on impact
719 force of low-speed droplets colliding with solid surface. *Exp. Fluids* **60** (4), 64.
- 720 ZHENG, S., DILLAVOU, S. & KOLINSKI, J. M. 2021 Air mediates the impact of a compliant
721 hemisphere on a rigid smooth surface. *Soft Matter* **17** (14), 3813–3819.